Local subcell monolithic DG/FV methods for nonlinear shallow-water models with source terms

Sacha Cardonna, Ali Haidar, Fabien Marche & François Vilar

December 22, 2025

Abstract. This paper contains several new contributions to the numerical approximation of shallow-water equations. We introduce a high-order *local subcell monolithic DG/FV* discretization method for the approximation of nonlinear free-surface shallow-water equations with source terms. This encompasses both nonlinear hyperbolic shallow-water equations (also known as *Saint-Venant* equations) and weakly-dispersive fully-nonlinear equations (known as *Green-Naghdi* equations), approximating the general free-surface water-wave equations in the shallow-water flow regime. The method is grounded on a classical Discontinuous Galerkin (DG) formulation, written as a particular Finite Volume (FV) discretization on a sub-partition, involving reconstructed high-order interface numerical fluxes. In the present work, we investigate the important issue of source terms discretization in the framework of such local subcell monolithic DG/FV strategies, focusing on the bathymetry source terms, and also higher-order differential source terms coming from dispersive corrections for higher-order asymptotic models. The originality of the method is the introduction of *a priori* blended fluxes, which are convex combinations of the so-called high-order reconstructed fluxes and low-order FV fluxes. The blending coefficients are adaptively computed for each subcell interface to enforce relevant convex properties at the discrete level, including water-height positivity. Starting from the DG piecewise polynomial approximation, the bathymetry source term is also discretized at the subcell level, and we prove that a suitable well-balanced property, ensuring the preservation of motionless steady-states, can be achieved at the subcell-scale relying on some finely tuned combinations of various hydrostatic-like reconstructed states at lower/higher accuracy levels, simultaneously occurring at local and global scales. We also introduce an original and efficient combination of this new well-balanced local subcell monolithic DG/FV with a high-order *Internal Penalty discontinuous-Galerkin* method, in order to approximate the higher-order contributions appearing in the Green-Naghdi equations in a consistent and accurate way. We then conduct extensive evaluations of the resulting numerical methods, providing insights about the observed numerical convergence and the overall robustness, including the ability to preserve steady-states, to prevent nonphysical oscillations near discontinuities and to ensure the positivity of the water-height at the discrete level.

Contents

1. Introduction.

The NSW equations are one of the most popular models for the description of shallow-water flows in some particular flow regimes. These equations are extensively used for the study of hydraulic, geophysical or oceanographical problems related to wave propagation and transformations in nearshore areas. Compared to the (weakly dispersive) Boussinesq-type models, the hyperbolic nature of the NSW equations generally provides a precise depiction of steep-fronted flows, such as dam-breaks, flood waves, and bore propagation in surf zones. Extensively used in the study of water ressources and coastal engineering, this model has also proved its efficiency to investigate flows involving run-up and run-down on coastal structures and, for instance, predicting coastal inundations, see for instance [38, 51].

There exist quite a large number of numerical methods to approximate the solutions of the NSW equations, and we won't be able to provide an extensive view in a few lines but rather some guidelines in the corresponding literature. Since the 1960s, many efforts have been dedicated to numerical study of NSW equations' weak solutions, leading to Finite-Volumes (FV) methods [1, 2, 7, 30, 31, 84], Finite-Elements (FE) methods [6, 62, 67, 77], spectral methods [43, 56, 64] or residual distribution methods [3]. Notably, Godunov-type FV methods receive acclaim for their minimal computational expense and shock-capturing capacity, crucial for maintaining the integrity of discontinuous or steep gradients found in sharp-fronted and trans-critical shallow water flows, see among others [4, 8, 12, 15, 33, 46, 54, 59, 63, 71, 76]. However, FV methods generally exhibit low accuracy, at least without introducing elaborated reconstruction methods based on larger stencils.
Discontinuous Galerkin (DG) methods are high-order in nature and have recently surged in popularity for approximating solutions to various linear and nonlinear Partial Differential Equations (PDEs). By combining several features usually associated with FE, FV or spectral methods, DG methods have demonstrated several successes across numerous computational domains. They enable an arbitrary spatial order of accuracy, rely on compact stencils, are geometrically flexible (geometries and meshes) and h/p adaptative. Additionally, they easily allow concurrency programming and generally exhibit some local conservation and strong-stability properties. We refer the interested reader to [52, 70] for pioneering works, and to [21] for a general introduction to the various aspects of the DG methods. However, despite becoming sufficiently mature to handle realistic problems and their ability to successfully address various complex modelizations, DG methods notably suffer from nonlinear stability issues. Specifically, high-order DG methods may generate spurious oscillations near discontinuities or steep gradients, known as the *Gibbs* phenomenon, potentially resulting in unstable or unaccurate solutions. Another significant challenge in approximating the NSW equations with high-order DG methods is to maintain the water-height positivity in the vicinity of singularities associated with vacuum, due to the use of oscillating polynomials. Such issue may arise in situations involving alternative wet and dry areas, including the study of flood waves or run-up over coastal shores.

In recent years, various attempts have been pointed out to help stabilizing high-order approximations: these may be broadly categorized under the two *a priori* and *a posteriori* paradigms. The *a priori* approaches involve pre-emptive corrections: troubled zone indicators identify where corrections are needed [68], before advancing the numerical solution. Then, efforts are directed at the numerical solution or scheme to ensure progression to the next time step. Several methods include *artificial viscosity* [37, 47, 65, 78], borrowing from streamline upwind Petrov Galerkin (SUPG) and Galerkin least-squares methods, and popular limiting techniques like slope and moment limiters [10, 18, 25, 48, 53], which sequentially scale the different moments of the polynomial solution, preserving solution accuracy and boundedness near discontinuities. Furthermore, (H)WENO limiting procedures [5, 69, 87, 88] and solution filtering methods [60, 66, 75, 79] are employed to address spurious oscillations, with recent popularity in subcell FV shock capturing techniques within DG schemes [14, 19, 74].

While the aforementioned subcell FV correction techniques are *a priori*, a wide range of *a posteriori* subcell corrections has also gained considerable popularity. Within the *a posteriori* paradigm, an uncorrected candidate solution at the new time step is first computed. This solution is then assessed against a set of admissibility criteria (*e.g.* positivity, discrete maximum principle). If the criteria are satisfied, the candidate solution is kept; otherwise, it is locally recomputed using a more robust scheme. Notably, a posteriori procedures inherently preserve maximum principles and positivity, provided that the correction scheme itself does so [17, 23, 24]. Among recent *a posteriori* approaches are the MOOD technique [24], which progressively reduces the approximation order of the numerical scheme until admissibility is recovered, and subcell FV corrections applied in an *a posteriori* fashion [26]. The latter rely on subdividing each cell into subcells, applying a robust first-order FV (or alternative) scheme on each subcell, and subsequently reconstructing a high-order polynomial over the original cell. Such *a posteriori* stabilizations have demonstrated remarkable effectiveness in the context of shallow water simulations, see for instance [32, 42, 58]. However, whether applied *a priori* or *a posteriori*, these correction strategies typically modify the high-order DG polynomial globally within troubled cells, which may compromise the accuracy achievable on coarse meshes.

To address this limitation, a new conservative technique was introduced in [80, 82], designed to modify the DG numerical solution only locally at the subcell level. The method aims at preventing non-admissible solutions, preserving maximum principles and positivity for systems, and avoiding code failures, while maintaining high accuracy and conservation at the subcell scale. By restricting corrections to a minimal number of troubled subcells, the procedure effectively limits spurious oscillations and preserves both high-order accuracy and subcell resolution. Importantly, the approach is parameter-free and naturally adapts from second order to arbitrarily high orders. When applied to the NSW equations [40, 41], the method relies on specific local flux corrections at the subcell level, combined with *a posteriori* admissibility detectors. Despite their excellent performance across a broad range of problems, *a posteriori* strategies remain challenging both to implement and to analyze. Moreover, in such approaches, the solution in problematic subcells is typically recomputed using a purely first-order FV scheme, whereas a more effective strategy could involve a local combination of high-order DG and low-order FV discretizations. These considerations motivated the extension of the aforementioned local subcell correction strategy to a fully *a priori* framework.

In [81], building upon the analytical reformulation of high-order DG schemes as FV-like schemes defined on a subgrid, a new class of methods was introduced that combines, at the subcell level, a high-order DG discretization with a first-order FV scheme. These blended approaches, referred to as local subcell monolithic DG/FV schemes, are fully *a priori* and allow the enforcement of arbitrary convex admissibility properties. In addition, [81] provides an in-depth analysis of entropy stability within this novel local subcell monolithic framework. In parallel, several other monolithic approaches have been proposed in recent years, see for instance [49, 55, 61, 72, 73, 85] and references therein. In these methods, high-order schemes, such as DG spectral element methods (DGSEM) based on Summation-By-Parts (SBP) quadrature and flux collocation [55, 72, 73, 85], or continuous Galerkin discretizations [49, 61], are blended, at a scale smaller than the cell, with a low-order scheme to ensure that the numerical solution remains within a convex admissible set. For instance, in [55, 72], local subcell monolithic DGSEM/FV schemes are presented, closely related in spirit to [81]. The key distinction lies in the fact that the Gauss-Lobatto solution representation and flux collocation, while ensuring SBP properties, mainly restrict these approaches either to one spatial dimension or to tensor-product multi-dimensional settings on Cartesian grids. In contrast, the theoretical framework developed in [82], based on a general FV-like reformulation of DG schemes, is applicable to arbitrary spatial dimensions, unstructured meshes, and generic cell subdivisions. Let us nonetheless mention that successful extensions of these monolithic SBP DGSEM to unstructured grids composed of triangles have been carried out, in particular in [85] where entropy-stable DGSEM are blended with a low-order scheme to ensure positivity of the water height. However, the resulting formulation does not rely anymore on an explicit subcell structure. Instead, the low-order component is based on the solution of a graph Laplacian problem defined on a specific connectivity graph, rather than on a standard first-order FV scheme based on subcells.

Following the path of the novel local subcell monolithic method presented in [81], we introduce here a new discrete formulation with an arbitrary order of accuracy for the NSW equations relying on the definition of new blended fluxes, which are convex combination of higher-order reconstructed fluxes with first-order FV fluxes. The blending coefficient being computed at each step of time on each subcell interface, ensure water-height positivity. We also show that such an approach may be introduced while preserving the important class of motionless steady states slutions at the subcell level, provided the use of a *two-scales* hydrostatic reconstruction-like strategy, operating both at the cell and the subcell levels, adapting the ideas of [27, 29]. We

also show that such a stabilizing strategy may be extended to more elaborated shallow-water models, including weakly dispersive shallow-water asymptotics, like the Boussinesq or the Green-Naghdi (GN) equations, using an IP-DG high-order method for the associated elliptic sub-problems. In particular, we describe in details a coupling strategy between the proposed local subcell DG/FV monolithic method and a SWIP-DG method recently introduced in [86] for the GN equations, based on a suitable combination of projection and averaging operators. Next, we assess the ability of this new family of schemes, called monolithic DG-FV convex property preserving schemes, to remove nonphysical instabilities in the vicinity of singularities for the NSW equations, and ensure that the mean values of the water height on the sub-partition remain positive. We highlight, on several test-cases, the particularly interesting subcell resolution ability of the resulting scheme, which allows to accurately capture and track the wet-dry fronts time-evolutions even in the interior domain of some larger mesh-elements.

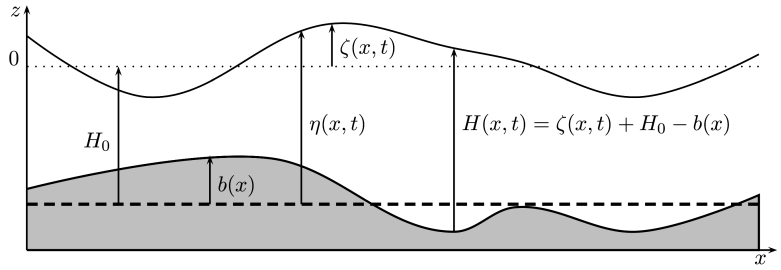

Figure 1: Main notations for free surface flows.

2. Continuous and discrete settings

2.1. Shallow-water models

Given a smooth parameterization b of the bathymetry variations, denoting by H the water height, u the horizontal (depth-averaged) velocity and $q = Hu$ the horizontal discharge, and defining the total free-surface elevation as $\eta := H + b$, see Fig. 1, we consider some shallow-water models, which may be commonly expressed as systems of partial differential equations of the form:

$$\partial_t \mathbf{v} + \partial_x \mathbf{F}(\mathbf{v}, b) = \mathbf{B}[b](\mathbf{v}) + \mathfrak{D}[H, b](\mathbf{v}), \tag{1}$$

supplemented with some initial-data $\mathbf{v}(\cdot, 0) := \mathbf{v}^0$ and where:

- $\mathbb{R} \times \mathbb{R}_+ \ni (x, t) \mapsto \mathbf{v}(x, t) := (\eta, q)(x, t) \in \mathscr{H}_b^+$ gathers the chosen flow description variables, with

$$\mathscr{H}_b^+ := \{(\eta, q) \in \mathbb{R}^2 \mid H := \eta - b \geq 0\},$$

- $\mathscr{H}_b^+ \times \mathbb{R} \ni (\mathbf{v}, b) \mapsto \mathbf{F}(\mathbf{v}, b) := \left(q,\ uq + \frac{1}{2}\mathrm{g}(\eta^2 - 2\eta b)\right)^t \in \mathbb{R}^2$ is the (nonlinear) flux function, given here in the pre-balanced form. We recall that the pre-balanced formulation of the flux relies on the following identity:

$$gH\partial_x \eta = \frac{1}{2} g \partial_x (\eta^2 - 2\eta b) + g\eta \partial_x b.$$

  ,

- $\mathscr{H}_b^+ \ni \mathbf{v} \mapsto \mathbf{B}[b](\mathbf{v}) := (0, -\mathrm{g}\eta\, b')^t \in \mathbb{R}^2$ stands for the bathymetry source term,
- $\mathscr{H}_b^+ \ni \mathbf{v} \mapsto \mathfrak{D}[H, b](\mathbf{v}) \in \mathbb{R}^2$ stands for higher-order differential operator acting on the flow variables $\mathbf{v}$, possibly including second-order diffusive viscosity terms and third-order dispersive non-hydrostatic terms.

  As an example, we investigate the later case for the GN model [36], written in the formulation introduced in [16], which fits the current framework, by setting:

$$\mathfrak{D}[H, b](\mathbf{v}) := -\Big(0, (1 + \mathcal{T}[H, b])^{-1} \mathbb{Q}[H, b](\mathbf{v}) - gH\partial_x \eta\Big), \tag{2}$$

where $\mathcal{T}[H,b]$ is a linear (invertible) operator (with nonlinear terms with respect to H and its derivatives) defined for any $w \in \mathrm{H}^2(\mathbb{R})$ (where $\mathrm{H}^s(\mathbb{R})$ denotes the Sobolev space of functions $v \in L^2(\mathbb{R})$ whose weak derivatives up to order s have a finite L^2-norm), as follows:

$$(1+\mathcal{T}[H,b])w \coloneqq \Big(H + \mathcal{S}_1[H,b]^\star H \mathcal{S}_1[H,b] + \mathcal{S}_2[b]^\star H \mathcal{S}_2[b]\Big)\frac{w}{H}.$$

In the previous definition, $\mathcal{S}_1[H,b]^\star$ and $\mathcal{S}_2[b]^\star$ stand for the respective adjoint operators of:

$$\mathcal{S}_1[H,b]w := \frac{H}{\sqrt{3}}\partial_x - \frac{\sqrt{3}}{2}\partial_x b, \qquad \mathcal{S}_2[b]w := \frac{1}{2}\partial_x b,$$

and the nonlinear operator $\mathfrak{Q}[H,b]$ is defined for all sufficiently smooth scalar-valued functions w as follows:

$$\mathfrak{Q}[H,b](\mathbf{v}) := gH\partial_x\eta + H(-2\mathcal{R}_1[H,b]((\partial_x w)^2) + \mathcal{R}_2[H,b]((w\partial_x)^2 b)), \tag{3}$$

with

$$\mathcal{R}_1[H,b]w := -\frac{1}{3H}\partial_x(H^3 w) - \frac{H}{2}w\partial_x b, \qquad \mathcal{R}_2[H,b]w := \frac{1}{2H}\partial_x(H^2 w) + w\partial_x b.$$

Remark 2.1. *Various algebraic source terms may also be considered like for instance nonlinear roughness bed-friction stresses terms. We recall that friction-driven stability issues may occur when $H \to 0$ and some suitable numerical treatment may be applied, like the one proposed in [9, 28] for instance.*

Remark 2.2. *Considering the homogeneous NSW equations ($\mathbf{B}[b](\mathbf{v}) = \mathfrak{D}[H,b](\mathbf{v}) = 0$), and taking $\mathbf{v}^0 \in (H^s(\mathbb{R}))^2$ with $s > 1 + d/2$ ($d = 1$ being the horizontal space dimension), the study of regular solutions to the Initial Value Problem (IVP) problem associated with (1) falls into the class of Cauchy problems for Friedrichs-symmetrizable systems and is locally well-posed in $\mathcal{C}((0,T),(H^s(\mathbb{R}))^2)$, see for instance [45]. Considering the GN equations, we refer to [44] for the invertibility of $(1+\mathcal{T}[H,b])$ and a long-time existence result for regular solutions from $\mathbf{v}^0 \in H^s(\mathbb{R}) \times H^{s+1}(\mathbb{R})$ in the $d = 1$ case. When bathymetry variations are accounted for, then the previous result still holds for $b \in \mathcal{C}^\infty_{\mathrm{b}}(\mathbb{R})$ (infinitely differentiable functions uniformly bounded together with all their derivatives).*

Remark 2.3. *As pointed out in [86], a convenient and exactly equivalent formulation for the GN equations reads as follows:*

$$\partial_t \mathbf{v} + \partial_x \mathbf{F}(\mathbf{v}, b) = \mathbf{B}[b](\mathbf{v}) + \mathbf{D}[H](\mathbf{v}, \Lambda), \tag{4}$$

where the previous higher-order term is replaced by the following (mostly algebraic) new one:

$$\mathbf{D}[H](\mathbf{v},\Lambda) \coloneqq \Big(0,\ gH\partial_x\eta - H\Lambda\Big), \tag{5}$$

the auxiliary variable Λ being obtained as the solution of a second-order linear differential elliptic problem:

$$\mathscr{L}[H,b]\Lambda = \mathfrak{Q}[H,b](\mathbf{v}), \tag{6}$$

with:

$$\mathscr{L}[H,b] \coloneqq H + \mathcal{S}_1[H,b]^\star H \mathcal{S}_1[H,b] + \mathcal{S}_2[b]^\star H \mathcal{S}_2[b]. \tag{7}$$

Such operator, supplemented with suitable boundary conditions when bounded domain are considered, see the next Remark 2.4, allows some convenient numerical decoupling of differential operators approximations. This last formulation is used in the remainder of this work.

Remark 2.4. *In practice, the numerical solution of (4)-(6) is sought in the closure of a bounded spatial domain $\overline{\Omega} \subset \mathbb{R}$. To properly close this system, appropriate boundary conditions must be prescribed not only for the primal variables $\mathbf{v} := (\eta, q)$ but also for the auxiliary variable Λ, ensuring that the corresponding discrete problem is well-defined on Ω. In this work, we consider only periodic or the so-called "solid-wall" conditions (i.e. homogeneous Neumann on η and Λ, homogeneous Dirichlet on q) boundary conditions.*

2.2. Discrete setting

Mesh and related polynomial approximation

Let $\Omega \subset \mathbb{R}$ denote the computational domain (interval), with boundary $\partial\Omega$. We consider the following partition $\mathscr{T}_h := \{\omega_1, \dots, \omega_{n_{\rm el}}\} \subset \Omega$ of open disjoint elements ω of boundary $\partial\omega$ such that

$$\overline{\Omega} = \bigcup_{\omega \in \mathscr{T}_h} \overline{\omega}.$$

This partition is characterized by the mesh size $h := \max_{\omega_i \in \mathscr{T}_h} h_i$ where h_i is the size of ω_i. For a given element ω_i, we also note $\omega_i := [x_{i-\frac{1}{2}}, x_{i+\frac{1}{2}}]$ and x_i its barycenter. For any integer $k \geq 0$, let us define the broken-polynomials space:

$$\mathbb{P}^k(\mathscr{T}_h) := \{v \in L^2(\Omega) \mid \forall \omega \in \mathscr{T}_h,\ v_{|\omega} \in \mathbb{P}^k(\omega)\},$$

where $\mathbb{P}^k(\omega)$ denotes the space of polynomials in ω of total degree at most k, with $\dim \mathbb{P}^k(\omega) = k+1$. Piecewise polynomial functions belonging to some broken-polynomial space $\mathbb{P}^k(\mathscr{T}_h)$ are denoted with a subscript h in the following, and for any $v_h \in \mathbb{P}^k(\mathscr{T}_h)$, and for all $\omega_i \in \mathscr{T}_h$, we use the shortcut $v_h^i := v_{h_{|\omega_i}}$. For any $\omega_i \in \mathscr{T}_h$, a basis for $\mathbb{P}^k(\omega_i)$ is denoted by

$$\mathbf{\Psi}_{\omega_i} := \{\psi_j^i\}_{j \in [\![1,k+1]\!]}, \tag{8}$$

and for $v_h^i \in \mathbb{P}^k(\omega_i)$, $\underline{v}^i := \left\{\underline{v}_j^i,\ j \in [\![1, k+1]\!]\right\}$ stand for the *local* degrees of freedom associated with ω_i, introduced as follows:

$$v_h^i := \sum_{j=1}^{k+1} \underline{v}_j^i \psi_j^i.$$

We also denote by $\underline{v} := \left\{\underline{v}^i,\ i \in [\![1, n_{\rm el}]\!]\right\}$ the *global* degrees of freedom of v_h. For $\omega_i \in \mathscr{T}_h$, we denote by p_i^k the L^2-orthogonal projector onto $\mathbb{P}^k(\omega_i)$ and p_h^k the global L^2-orthogonal projector onto $\mathbb{P}^k(\mathscr{T}_h)$, gathering all the local L^2 projectors p_i^k. We also define the broken gradient operator $\nabla_h^k \colon \mathbb{P}^k(\mathscr{T}_h) \to \mathbb{P}^{k-1}(\mathscr{T}_h)$ such that, for all $v_h \in \mathbb{P}^k(\mathscr{T}_h)$:

$$(\nabla_h^k v_h)_{|\omega} := \partial_x(v_{h|\omega}), \qquad \forall \omega \in \mathscr{T}_h.$$

Seeking for approximate solutions of (1), the next sections are devoted to the computation of $\mathbf{v}_h := (\eta_h, q_h)$, such that for any time value, $\mathbf{v}_h(\cdot, t) \in (\mathbb{P}^k(\mathscr{T}_h))^2$. For any given $\mathbf{v}_h \in (\mathbb{P}^k(\mathscr{T}_h))^2$, and for the sake of simplicity, we generally use the shortcuts $\mathbf{v}_{i\pm\frac{1}{2}}^{\mp} := v_h^i(x_{i\pm\frac{1}{2}})$ to describe its left and right traces at the mesh interfaces $x_{i\pm\frac{1}{2}}$.

Sub-mesh and related discrete operators

Let us divide the initial mesh into subcells: for any given mesh element $\omega_i \in \mathscr{T}_h$, we introduce a sub-partition $\mathscr{T}_{\omega_i}^k$ into $k+1$ open disjoint subcells:

$$\overline{\omega}_i := \bigcup_{m=1}^{k+1} \overline{S_m^i},$$

where the subcell $S_m^i := [\widetilde{x}_{m-\frac{1}{2}}^i, \widetilde{x}_{m+\frac{1}{2}}^i]$ is of size $|S_m^i| = |\widetilde{x}_{i+\frac{1}{2}}^i - \widetilde{x}_{i-\frac{1}{2}}^i|$, with the convention $\widetilde{x}_{\frac{1}{2}}^i = x_{i-\frac{1}{2}}$ and $\widetilde{x}_{k+\frac{3}{2}}^i = x_{i+\frac{1}{2}}$. When considering a sequence of neighboring element ω_{i-1}, ω_i and ω_{i+1}, we may use the convenient convention $S_0^i := S_{k+1}^{i-1}$ and $S_{k+2}^i := S_1^{i+1}$.

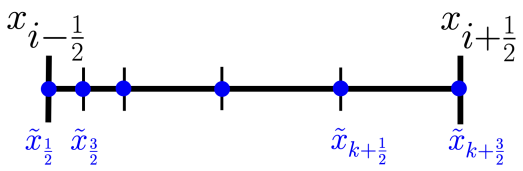

Figure 2: Subcell decomposition of ω_i through $k+2$ flux points.

For any given $\omega_i \in \mathscr{T}_h$, let us introduce the set of piecewise-constant functions on the sub-mesh:

$$\mathbb{P}^0(\mathscr{T}^k_{\omega_i}) := \{v \in L^\infty(\omega_i) \mid \forall S^i_m \in \mathscr{T}^k_{\omega_i},\ v_{|S^i_m} \in \mathbb{P}^0(S^i_m)\},$$

together with the subcell-indicator functions

$$\{\mathbb{1}^i_m \mid m \in [\![1, k+1]\!]\},$$

such that $\mathbb{1}^i_m(x) := 1$ if $x \in S^i_m$, and 0 otherwise, allowing to define the mean-value operator $\overline{\pi}^k_i$ onto $\mathbb{P}^0(\mathscr{T}^k_{\omega_i})$ such that

$$\mathbb{P}^k(\omega_i) \ni v^i_h \mapsto \overline{\pi}^k_i \circ v^i_h := \sum_{m=1}^{k+1} \overline{v}^i_m \mathbb{1}^i_m =: \overline{v}^i_h \in \mathbb{P}^0(\mathscr{T}^k_{\omega_i}),$$

where

$$\{\overline{v}^i_m,\ m \in [\![1, k+1]\!]\} =: \overline{v}^i,$$

is the collection of piecewise-constant components defined as the mean-values of v^i_h on the subcells belonging to the subdivision $\mathscr{T}^k_{\omega_i}$, and called *sub-mean values*. In order to reach a global description of subcells and related operators, with concise notations, we gather the local subcells partitions and define the associated global approximation space as follows:

$$\widetilde{\mathscr{T}_h} := \bigcup_{\omega \in \mathscr{T}_h} \mathscr{T}^k_\omega, \qquad \mathbb{P}^0(\widetilde{\mathscr{T}_h}) := \bigtimes_{\omega \in \mathscr{T}_h} \mathbb{P}^0(\mathscr{T}^k_\omega).$$

The global projector onto $\mathbb{P}^0(\widetilde{\mathscr{T}_h})$, obtained by gathering the local ones $\overline{\pi}^k_i$, is denoted by $\overline{\pi}^k_h$. Note that $\overline{\pi}^k_h$ can be extended to larger functional spaces (typically $\mathrm{H}^s(\mathbb{R})$, $s > 1 + d/2$ for the initial data, and $\mathscr{C}^\infty_{\mathrm{b}}(\mathbb{R})$ for the bathymetry) and denoted $\widetilde{\pi}^k_h$. In what follows, piecewise-constant functions belonging to $\mathbb{P}^0(\widetilde{\mathscr{T}_h})$ are denoted with an overline $\bar{}$ and a subscript h, and for any $\overline{v}_h \in \mathbb{P}^0(\widetilde{\mathscr{T}_h})$, and for all $S^i_m \in \widetilde{\mathscr{T}_h}$, we obviously have the identity $\overline{v}^i_m = \overline{v}_{h|S^i_m}$.

Remark 2.5. *It can be shown that $\overline{\pi}^k_i : \mathbb{P}^k(\omega_i) \to \mathbb{P}^0(\mathscr{T}^k_{\omega_i})$ is one-to-one and onto. For implementation purpose, the associated local transformation matrix $\mathbb{P}_i = \left(\pi^i_{m,p}\right)_{(m,p)\in[\![1,\,k+1]\!]^2}$ is defined as:*

$$\pi^i_{m,p} = \frac{1}{|S^i_m|} \int_{S^i_m} \psi^i_p \mathrm{d}x, \qquad \forall\, (m,p) \in [\![1,\, k+1]\!]^2, \tag{9}$$

and we have the transformation relations:

$$\mathbb{P}_i\, \underline{v}^{\,i} = \overline{v}^i \quad \textit{and} \quad \mathbb{P}_i^{-1}\, \overline{v}^i = \underline{v}^i. \tag{10}$$

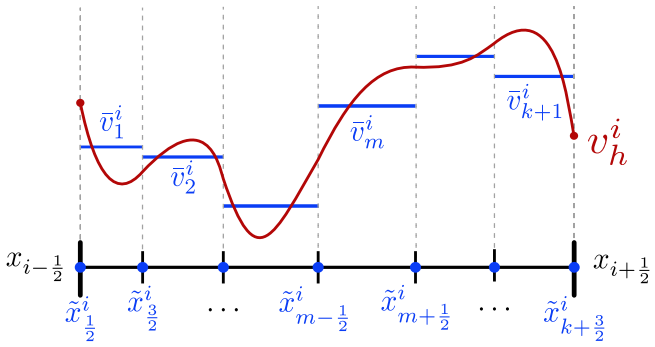

Figure 3: Piecewise polynomial function v^i_h and associated sub-mean values

Time discretization and time-marching algorithm.

For a given final time $T > 0$, we also introduce a general partition of the time domain $0 =: t^0 < t^1 < \cdots < t^n < \cdots < t^N := T$, and the adaptative time step $\Delta t^n \in \mathbb{R}_+$ such that, for any $n \geq 0$, $t^{n+1} = t^n + \Delta t^n$. Time

integration may be carried out using explicit *Strong Stability Preserving Runge-Kutta* schemes [35].

Introducing time-stepping algorithm leads to introduce some new time-related notations, with $\mathbf{v}_h^n := \mathbf{v}_h(\cdot, t^n)$ and $\overline{\mathbf{v}}_h^n := \overline{\pi}_h^k \circ \mathbf{v}_h^n =: (\overline{\eta}_h^n, \overline{q}_h^n)$ being the corresponding piecewise-constant function defined on the sub-mesh. We also denote by

$$\overline{\mathbf{v}}^{i,n} := \{\overline{\mathbf{v}}_m^{i,n},\ 1 \leq m \leq k+1\},$$

the collection of sub-mean values associated with ω_i at time t^n and we obviously have $\overline{\mathbf{v}}_m^{i,n} = \overline{\mathbf{v}}_{h|S_m^i}^n$. Note that when no confusions are possible, the superscripts i (cell-related) and n (time-related) may be suppressed, for the sake of simplicity. Then, considering the semi-discrete formulation written in operator form

$$\partial_t \mathbf{v}_h + \mathcal{N}_h(\mathbf{v}_h) = 0,$$

where $\mathcal{N}_h$ stands for the nonlinear operator allowing to compute the approximated residuals, and considering for instance the third-order SSP-RK scheme, we advance from time level n to $(n+1)$ with the third-order explicit scheme as follows:

$$\begin{aligned}
\mathbf{v}_h^{n,1} &= \mathbf{v}_h^n - \Delta t^n \mathcal{N}_h(\mathbf{v}_h^n),\\
\mathbf{v}_h^{n,2} &= \frac{1}{4}(3\mathbf{v}_h^n + \mathbf{v}_h^{n,1}) - \frac{\Delta t^n}{4}\mathcal{N}_h(\mathbf{v}_h^{n,1}),\\
\mathbf{v}_h^{n+1} &= \frac{1}{3}(\mathbf{v}_h^n + 2\mathbf{v}_h^{n,2}) - \frac{\Delta t^n}{3}\mathcal{N}_h(\mathbf{v}_h^{n,2}),
\end{aligned}$$

where $\mathbf{v}_h^{n,1}$ and $\mathbf{v}_h^{n,2}$ are the solution obtained at intermediate stages, and the initial data $\mathbf{v}_h^0$ is yet to be defined (see §4.1 and the consistency with the bathymetry variations approximation). As our monolithic scheme both uses DG schemes on primal cells $\omega_i \in \mathscr{T}_h$ and FV schemes on subcells $S_m^i \in \mathscr{T}_\omega$, the time step Δt^n is computed adaptively using the following CFL condition:

$$\Delta t^n := \frac{\min\limits_{\omega_i \in \mathscr{T}_h}\left(\dfrac{h_i}{2k+1}, \min\limits_{S_m^i \in \mathscr{T}_{\omega_i}^k} |S_m^i|\right)}{\sigma}, \qquad \sigma := \max_{\omega_i \in \mathscr{T}_h} \max_{m \in [\![1,\, k+1]\!]} \left(\left|\overline{u}_m^i\right| + \sqrt{\mathrm{g}\overline{H}_m^i}\right). \tag{11}$$

3. Local subcell monolithic DG/FV for homogeneous system

Looking at the homogeneous NSW equations, we observe that the flux definition may be simplified as follows:

$$\mathscr{H}_b^+ \ni \mathbf{v} \mapsto \mathbf{F}(\mathbf{v}) := \left(q,\ uq + \frac{\mathrm{g}H^2}{2}\right)^t \in \mathbb{R}^2.$$

3.1. A hierarchy of numerical fluxes

In what follows, we manipulate a collection of various numerical fluxes defined on mesh or sub-mesh interfaces that we find useful to gather their definitions in one place, for further referencing:

- the global Lax-Friedrichs (LF) flux is used throughout this work and is defined as follows:

$$(\mathscr{H}_b^+)^2 \ni (\mathbf{v}_l, \mathbf{v}_r) \mapsto \boldsymbol{\mathcal{F}}(\mathbf{v}_l, \mathbf{v}_r) := \frac{1}{2}\left(\mathbf{F}(\mathbf{v}_r) + \mathbf{F}(\mathbf{v}_l) - \sigma(\mathbf{v}_r - \mathbf{v}_l)\right).$$

  Let us emphasize that any other consistent and positive numerical fluxes, including the local LF, the HHL / HLLC or kinetic-based fluxes, may be used.

- the lowest-order subcell FV fluxes $\left\{\boldsymbol{\mathcal{F}}^{\mathrm{FV}}\right\}_{m \in [\![1,k]\!]}$: these first-order fluxes may only be evaluated at the *interfaces* between neighboring subcells, within a mesh element, and are given by

$$\boldsymbol{\mathcal{F}}^{\mathrm{FV}}_{m+\frac{1}{2}} := \boldsymbol{\mathcal{F}}(\overline{\mathbf{v}}_m, \overline{\mathbf{v}}_{m+1}), \qquad \boldsymbol{\mathcal{F}}^{\mathrm{FV}}_{m-\frac{1}{2}} := \boldsymbol{\mathcal{F}}(\overline{\mathbf{v}}_{m-1}, \overline{\mathbf{v}}_m),$$

- the higher-order DG fluxes $\boldsymbol{\mathcal{F}}^{\mathrm{DG}}_{i\pm\frac{1}{2}}$: these fluxes may only be evaluated at the *interfaces* between two neighboring mesh elements as follows:

$$\boldsymbol{\mathcal{F}}^{\mathrm{DG}}_{i\pm\frac{1}{2}} := \boldsymbol{\mathcal{F}}\left(\mathbf{v}^-_{i\pm\frac{1}{2}}, \mathbf{v}^+_{i\pm\frac{1}{2}}\right),$$

  where $\mathbf{v}^\pm_{i\pm\frac{1}{2}}$ are the left and right traces of (polynomial) $\mathbf{v}_h$ at mesh interface $i+\frac{1}{2}$,

♯ the *reconstructed* subcell fluxes $\left\{\widehat{\mathbf{F}}^i_{m+\frac{1}{2}}\right\}_{m\in[\![0,k+1]\!]}$: these fluxes are introduced below within the equivalency formulation (15) and aim at locally mimicking the behavior of an "in-cell" FV scheme, giving exactly and equivalently the DG approximated solution, and are defined as follows:

$$\widehat{\mathbf{F}}^i_{m+\frac{1}{2}} = \mathbf{F}^i_h(\widetilde{x}^i_{m+\frac{1}{2}}) - C^{i-\frac{1}{2}}_{m+\frac{1}{2}}\left(\mathbf{F}^i_h(x_{i-\frac{1}{2}}) - \boldsymbol{\mathscr{F}}^{\mathrm{DG}}_{i-\frac{1}{2}}\right) - C^{i+\frac{1}{2}}_{m+\frac{1}{2}}\left(\mathbf{F}^i_h(x_{i+\frac{1}{2}}) - \boldsymbol{\mathscr{F}}^{\mathrm{DG}}_{i+\frac{1}{2}}\right), \tag{12}$$

where the coefficients $C^{i\pm\frac{1}{2}}_{m+\frac{1}{2}}$ are explicitly given in [81], and $\mathbf{F}^i_h := p^k_i \circ \mathbf{F}(v^i_h)$ corresponds to the L^2 projection of the interior flux,

♯ the *blended* subcell fluxes $\left\{\widetilde{\mathbf{F}}^i_{m+\frac{1}{2}}\right\}_{m\in[\![0,k+1]\!]}$: these fluxes are defined as convex combinations of the lowest-order subcell FV fluxes $\boldsymbol{\mathscr{F}}^{\mathrm{FV}}$ and the *reconstructed* subcell fluxes $\widehat{\mathbf{F}}^i_{m+\frac{1}{2}}$. For $\omega_i = [x_{i-\frac{1}{2}}, x_{i+\frac{1}{2}}] \in \mathscr{T}_h$, we introduce:

$$\widetilde{\mathbf{F}}^i_{m+\frac{1}{2}} \coloneqq \boldsymbol{\mathscr{F}}^{\mathrm{FV}}_{m+\frac{1}{2}} + \Theta_{m+\frac{1}{2}}\left(\widehat{\mathbf{F}}^i_{m+\frac{1}{2}} - \boldsymbol{\mathscr{F}}^{\mathrm{FV}}_{m+\frac{1}{2}}\right),$$

with $\Theta_{m+\frac{1}{2}} \in [0,1]$. The computation of such *blended coefficients* to ensure different desired properties is detailed below.

3.2. DG and subcell reformulation

We recall, see for instance [40], that a straightforward semi-discrete global DG approximation for the homogeneous NSW equations may read as follows: find $\mathbf{v}_h \coloneqq (\eta_h, q_h) \in (\mathbb{P}^k(\mathscr{T}_h))^2$ such that, for all $\varphi \in \mathbb{P}^k(\mathscr{T}_h)$:

$$\sum_{\omega_i\in\mathscr{T}_h}\int_{\omega_i}\partial_t\mathbf{v}_h\varphi\,\mathrm{d}x - \sum_{\omega_i\in\mathscr{T}_h}\int_{\omega_i}\mathbf{F}(\mathbf{v}_h)\partial_x\varphi\,\mathrm{d}x + \sum_{\omega_i\in\mathscr{T}_h}\left[\varphi\boldsymbol{\mathscr{F}}^{\mathrm{DG}}\right]^{i+\frac{1}{2}}_{i-\frac{1}{2}} = 0, \tag{13}$$

which locally translates as: for all $\omega_i \in \mathscr{T}_h$, find $\mathbf{v}^i_h \coloneqq (\eta^i_h, q^i_h) \in (\mathbb{P}^k(\omega_i))^2$ such that, for all $\varphi \in \mathbb{P}^k(\omega_i)$

$$\int_{\omega_i}\partial_t\mathbf{v}^i_h\varphi\,\mathrm{d}x - \int_{\omega_i}\mathbf{F}(\mathbf{v}^i_h)\partial_x\varphi\,\mathrm{d}x + \left[\varphi\boldsymbol{\mathscr{F}}^{\mathrm{DG}}\right]^{i+\frac{1}{2}}_{i-\frac{1}{2}} = 0. \tag{14}$$

We also recall an essential result of [81], which states the equivalence between DG and a FV-like formulation on the sub-mesh:

Proposition 3.1. *For any given $\omega_i \in \mathscr{T}_h$, the local DG formulation (14) can be equivalently written as a FV-like scheme defined on the sub-mesh, as follows:*

$$\partial_t\overline{\mathbf{v}}^i_m = -\frac{1}{|S^i_m|}\left(\widehat{\mathbf{F}}^i_{m+\frac{1}{2}} - \widehat{\mathbf{F}}^i_{m-\frac{1}{2}}\right), \qquad \forall m \in [\![1, k+1]\!], \tag{15}$$

where the reconstructed fluxes $\widehat{\mathbf{F}}^i_{m\pm\frac{1}{2}}$ are defined in (12) and $\overline{\mathbf{v}}^i_m \coloneqq (\overline{\pi}^k_i \circ \mathbf{v}^i_h)_{|S^i_m}$.

Relying on the general formulation (13) and the equivalent local translation at the subcell level (15), and in the spirit of [40], we aim at building some robust numerical fluxes, at the subcell level, in order to enforce some nonlinear stability properties.

3.3. Local subcell monolithic method and blending coefficients

The main idea of the local subcell monolithic method is to substitute the *blended* fluxes for the *reconstructed* fluxes into the local subcell formulations (15), in order to provide some subcell scale flexibility to enforce nonlinear stability properties through suitable and adaptive computations of the local blending coefficients $\Theta_{m+\frac{1}{2}}$. Applying a first-order time-stepping algorithm for the sake of simplicity (any higher-order SSP-RK method may be used as well), we thus consider the local subcell monolithic formulations:

$$\overline{\mathbf{v}}^{i,n+1}_m = \overline{\mathbf{v}}^{i,n}_m - \frac{\Delta t^n}{|S^i_m|}\left(\widetilde{\mathbf{F}}^i_{m+\frac{1}{2}} - \widetilde{\mathbf{F}}^i_{m-\frac{1}{2}}\right), \qquad \forall m \in [\![1, k+1]\!], \qquad \forall i \in [\![1, n_{\mathrm{el}}]\!], \tag{16}$$

which is of course also conservative at the subcell level, and we are left with the computation of the blending coefficient $\{\Theta_{m+\frac{1}{2}}\}_{m\in[\![0,k+1]\!]}$. To achieve this, let us have a look first to the lowest-order scheme, obtained by uniformly setting $\Theta_{m+\frac{1}{2}}=0$:

$$\overline{\mathbf{v}}_m^{i,n+1}=\overline{\mathbf{v}}_m^{i,n}-\frac{\Delta t^n}{|S_m^i|}\left(\boldsymbol{\mathscr{F}}_{m+\frac{1}{2}}^{\mathrm{FV}}-\boldsymbol{\mathscr{F}}_{m-\frac{1}{2}}^{\mathrm{FV}}\right),\qquad\forall m\in[\![1,k+1]\!],\qquad\forall i\in[\![1,n_{\mathrm{el}}]\!],\tag{17}$$

and observe that (17) may be seen as a convex combination of flow-states defined at time-step n, as follows:

$$\overline{\mathbf{v}}_m^{n+1}=\left(1-\frac{2\Delta t^n}{|S_m|}\sigma\right)\overline{\mathbf{v}}_m^n+\frac{\sigma\Delta t^n}{|S_m|}\mathbf{v}_{m+\frac{1}{2}}^{*,-}+\frac{\sigma\Delta t^n}{|S_m|}\mathbf{v}_{m+\frac{1}{2}}^{*,+}.$$

These $\mathbf{v}_{m+\frac{1}{2}}^{*,\pm}$ are called *lowest-order intermediate Riemann flow-states*, and writes as follows

$$\mathbf{v}_{m\mp\frac{1}{2}}^{*,\pm}:=\overline{\mathbf{v}}_m^n\pm\frac{\boldsymbol{\mathscr{F}}_{m\mp\frac{1}{2}}^{\mathrm{FV},\pm}-\mathbf{F}(\overline{\mathbf{v}}_m^n)}{\sigma}.$$

Finally, it can be proved that $\mathbf{v}_{m\mp\frac{1}{2}}^{*,\pm}\in\mathscr{H}_b^+$, providing the CFL-like condition (11), see Appendix A.

Now, considering the case of higher-order blended fluxes, we observe in a similar way that (16) may be written as a combination of intermediate states defined at time-step n, as follows:

$$\overline{\mathbf{v}}_m^{n+1}=\left(1-\frac{2\Delta t^n}{|S_m|}\sigma\right)\overline{\mathbf{v}}_m^n+\frac{\sigma\Delta t^n}{|S_m|}\widetilde{\mathbf{v}}_{m+\frac{1}{2}}^{*,-}+\frac{\sigma\Delta t^n}{|S_m|}\widetilde{\mathbf{v}}_{m+\frac{1}{2}}^{*,+},\tag{18}$$

where the new *blended intermediate Riemann states* $\widetilde{\mathbf{v}}_{m+\frac{1}{2}}^{*,\pm}$ are defined as follows:

$$\widetilde{\mathbf{v}}_{m+\frac{1}{2}}^{*,\pm}:=\mathbf{v}_{m+\frac{1}{2}}^{*,\pm}\pm\Theta_{m+\frac{1}{2}}\left(\frac{\widehat{\mathbf{F}}_{m+\frac{1}{2}}-\boldsymbol{\mathscr{F}}_{m+\frac{1}{2}}^{\mathrm{FV}}}{\sigma}\right).\tag{19}$$

Hence, it is enough to sought the blended-coefficient values $\Theta_{m+\frac{1}{2}}$ such that the required convex properties are enforced on the *blended states* $\widetilde{\mathbf{v}}_{m+\frac{1}{2}}^{*,\pm}$.

Similarly to what has been previously done in the *a posteriori* context, [40, 80], we seek to:

- ♯ enforce a local maximum principle in the vicinity of singularities for the NSW equations, at the discrete subcell scale, in order to prevent the occurrence of spurious oscillations when discontinuities appear: an adaptive *Numerical Admissibility Detection* (NAD) may be applied at the *subcell* level - hence, the *SubNAD* naming of this sensor,
- ♯ ensure that the updated water-height remains non-negative at each time-step - or sub-step for RK time-stepping, and at the subcell level. This property, referred to as Physical Admissibility Detection (PAD), should be enforced while taking into account the bathymetry variations and is therefore temporarily postponed to the next section.

Subcell Numerical Admissibility Detection (subNAD)

We impose the updated sub-mean values to be bounded in a suitable local subset of the sub-mean values at previous time step (or previous sub-step for higher-order RK time-stepping). We also add the intermediate lowest-order states in this subset, and we aim at enforcing that, for $m\in[\![1,k+1]\!]$:

$$\min\left(\overline{\mathbf{v}}_{m-1}^{i,n},\overline{\mathbf{v}}_m^{i,n},\overline{\mathbf{v}}_{m+1}^{i,n},\mathbf{v}_{m-\frac{1}{2}}^{*,+},\mathbf{v}_{m+\frac{1}{2}}^{*,-}\right)\leq\overline{\mathbf{v}}_m^{i,n+1}\leq\max\left(\overline{\mathbf{v}}_{m-1}^{i,n},\overline{\mathbf{v}}_m^{i,n},\overline{\mathbf{v}}_{m+1}^{i,n},\mathbf{v}_{m-\frac{1}{2}}^{*,+},\mathbf{v}_{m+\frac{1}{2}}^{*,-}\right),\tag{20}$$

whith $\overline{\mathbf{v}}_0^{i,n}=\overline{\mathbf{v}}_{k+1}^{i-1,n}$ and $\overline{\mathbf{v}}_{k+2}^{i,n}=\overline{\mathbf{v}}_1^{i+1,n}$ as usual, see Appendix B for more details.

Remark 3.2. *This criterion should be supplemented with a relaxation procedure to exclude the smooth extrema from the troubled cells, i.e. uniformly enforce $\Theta_{m+\frac{1}{2}}=1$ when such an extrema occurred. We use, and refer the interested reader to, the relaxation procedure proposed and validated in [40, 81].*

The following expression of blending coefficient $\Theta^{\text{sNAD}}_{m+\frac{1}{2}}$ allows to ensure such a (convex) property:

Proposition 3.3. *The local subcell maximum principle (20) is satisfied as soon as the following inequalities are locally satisfied by the blending coefficients:*

$$\Theta_{m+\frac{1}{2}} \leq \Theta^{sNAD}_{m+\frac{1}{2}},$$

with:

$$\Theta^{\text{sNAD}}_{m+\frac{1}{2}} := \min\left(1, \left|\frac{\sigma}{\Delta\mathbf{F}^{(1)}_{m+\frac{1}{2}}}\right| \begin{cases} \min\left(\beta_{m+1} - \eta^{*,+}_{m+\frac{1}{2}},\ \eta^{*,-}_{m+\frac{1}{2}} - \alpha_m\right) & \text{if } \Delta\mathbf{F}^{(1)}_{m+\frac{1}{2}} > 0 \\ \min\left(\beta_m - \eta^{*,-}_{m+\frac{1}{2}},\ \eta^{*,+}_{m+\frac{1}{2}} - \alpha_{m+1}\right) & \text{if } \Delta\mathbf{F}^{(1)}_{m+\frac{1}{2}} < 0 \end{cases}\right),$$

where $\Delta\mathbf{F}^{(1)}_{m+\frac{1}{2}} := \widehat{\mathbf{F}}^{(1)}_{m+\frac{1}{2}} - \boldsymbol{\mathcal{F}}^{\text{FV},(1)}_{m+\frac{1}{2}}$ *stands for the first component of the flux (appearing in the mass-conservation equation), and dropping* $\pm$ *indices for sake of clarity, with*

$$\left\{\alpha_m, \beta_m\right\} := \left\{\min(\overline{\eta}_{m-1}, \overline{\eta}_m, \overline{\eta}_{m+1}, \eta^{*,+}_{m-\frac{1}{2}}, \eta^{*,-}_{m+\frac{1}{2}}),\ \max(\overline{\eta}_{m-1}, \overline{\eta}_m, \overline{\eta}_{m+1}, \eta^{*,+}_{m-\frac{1}{2}}, \eta^{*,-}_{m+\frac{1}{2}})\right\}.$$

Proof. See Appendix B. □

Remark 3.4. *We also show in §5, through various numerical evidences, that such a constraint effectively allows to get rid of most of the spurious oscillations, while accurately preserving the high-order accuracy wherever needed.*

The issue of enforcing the water-height non-negativity deserves to be studied while accounting for the possibly varying bathymetry and, as a consequence, is temporarily postponed to the next section.

4. Local subcell approximations of source terms

We investigate the issue of the discrete approximation, *in the local subcell framework*, of the *source terms*. We begin with the case of hyperbolic NSW equations with a bathymetry source term and focus on a compatible discretization with the preservation of motionless steady-states, and the admissibility of the discrete solutions. In a second time, we introduce a novel *combined local subcell monolithic DG/FV and SWIP-DG discrete formulation* in order to extend the discretization to the GN equations.

4.1. Bathymetry source term

Let us consider the following NSW equations with bathymetry source term:

$$\partial_t \mathbf{v} + \partial_x \mathbf{F}(\mathbf{v}, b) = \mathbf{B}[b](\mathbf{v}), \tag{21}$$

where $\mathbf{B}[b]$ is defined in Section 2.1. For further use, we introduce the following bathymetry approximations:

$$\overline{b}_h := \widetilde{\pi}^k_h b \in \mathbb{P}^0(\widetilde{\mathscr{T}_h}) \qquad \text{and} \qquad b_h := (\overline{\pi}^k_h)^{-1}\overline{b}_h \in \mathbb{P}^k(\mathscr{T}_h). \tag{22}$$

A new hierarchy of numerical fluxes and two-scales hydrostatic reconstruction

The occurrence of bathymetry has a global impact on the definition of the numerical fluxes hierarchy previously introduced in the homogeneous case. To account for the bathymetry variations while preserving the accuracy and allowing the resulting global scheme to be *well-balanced*, we have to modify the definition of bothhigh-order and low-order fluxes composing the so-called *blended fluxes*. Such a modification is inspired by the *hydrostatic reconstruction* initially introduced within FV schemes for NSW equations [4] and extended for the pre-balanced form in [29,54]. We emphasize that the distinctiveness of the proposed approach is that such a reconstruction has to be *performed not only at the cell scale, but also at the subcell scale*, with suitable intermediate reconstructed states, detailed below:

♯ the global LF numerical flux and bathymetry variations: the chosen interface flux has to account for the bathymetry variations from cell to cell or subcell to subcell, and is defined as follows:

$$(\mathscr{H}^+_b)^2 \times \mathbb{R} \ni (\mathbf{v}_l, \mathbf{v}_r, b) \mapsto \boldsymbol{\mathcal{F}}(\mathbf{v}_l, \mathbf{v}_r, b) := \frac{1}{2}\left(\mathbf{F}(\mathbf{v}_r, b) + \mathbf{F}(\mathbf{v}_l, b) - \sigma(\mathbf{v}_r - \mathbf{v}_l)\right), \tag{23}$$

♯ *modified* higher-order DG fluxes $\boldsymbol{\mathscr{F}}^{\mathrm{DG},\mp}_{i\pm\frac{1}{2}}$ and mesh-scale hydrostatic reconstruction: tThe higher-order fluxes are now designed relying on *high-order reconstructed traces* of the bathymetry performed *at the mesh scale* (*i.e.* at mesh elements interfaces). Let us define, for any mesh element $\omega_i \in \mathscr{T}_h$:

$$\widehat{b}_{i+\frac{1}{2}} := \check{b}_{i+\frac{1}{2}} - \max(0, \check{b}_{i+\frac{1}{2}} - \eta^-_{i+\frac{1}{2}}), \qquad \widehat{b}_{i-\frac{1}{2}} := \check{b}_{i-\frac{1}{2}} - \max(0, \check{b}_{i-\frac{1}{2}} - \eta^+_{i-\frac{1}{2}}),$$

with

$$\check{b}_{i\pm\frac{1}{2}} := \max\left(b^-_{i\pm\frac{1}{2}}, b^+_{i\pm\frac{1}{2}}\right),$$

and where $b^\pm_{i\pm\frac{1}{2}} \coloneqq b^i_h(x_{i\pm\frac{1}{2}})$ and $\eta^\pm_{i\pm\frac{1}{2}} \coloneqq \eta^i_h(x_{i\pm\frac{1}{2}})$. These reconstructed interface bathymetry values allow to introduce the following *reconstructed* water-height traces values:

$$\check{H}^\pm_{i+\frac{1}{2}} := \max(0, \eta^\pm_{i+\frac{1}{2}} - \check{b}_{i+\frac{1}{2}}) \quad \text{and} \quad \check{H}^\pm_{i-\frac{1}{2}} := \max(0, \eta^\pm_{i-\frac{1}{2}} - \check{b}_{i+\frac{1}{2}}),$$

together with the corresponding *reconstructed* flow-states $\check{\mathbf{v}}^\pm_{i\pm\frac{1}{2}}$, as follows:

$$\check{\eta}^\pm_{i+\frac{1}{2}} := \check{H}^\pm_{i+\frac{1}{2}} + \widehat{b}_{i+\frac{1}{2}} \quad \text{and} \quad \check{q}^\pm_{i+\frac{1}{2}} := \check{H}^\pm_{i+\frac{1}{2}} \frac{q^\pm_{i+\frac{1}{2}}}{H^\pm_{i+\frac{1}{2}}},$$

$$\check{\eta}^\pm_{i-\frac{1}{2}} := \check{H}^\pm_{i-\frac{1}{2}} + \widehat{b}_{i-\frac{1}{2}} \quad \text{and} \quad \check{q}^\pm_{i-\frac{1}{2}} := \check{H}^\pm_{i-\frac{1}{2}} \frac{q^\pm_{i-\frac{1}{2}}}{H^\pm_{i-\frac{1}{2}}}.$$

Using these reconstructed flow-states, some new high-order interface fluxes are defined:

$$\boldsymbol{\mathscr{F}}^{\mathrm{DG},-}_{i+\frac{1}{2}} := \boldsymbol{\mathscr{F}}\left(\check{\mathbf{v}}^-_{i+\frac{1}{2}}, \check{\mathbf{v}}^+_{i+\frac{1}{2}}, \widehat{b}_{i+\frac{1}{2}}\right) + \begin{pmatrix} 0 \\ g\check{\eta}^-_{i+\frac{1}{2}}\left(\widehat{b}_{i+\frac{1}{2}} - b^-_{i+\frac{1}{2}}\right) \end{pmatrix}, \tag{24}$$

$$\boldsymbol{\mathscr{F}}^{\mathrm{DG},+}_{i-\frac{1}{2}} := \boldsymbol{\mathscr{F}}\left(\check{\mathbf{v}}^-_{i-\frac{1}{2}}, \check{\mathbf{v}}^+_{i-\frac{1}{2}}, \widehat{b}_{i-\frac{1}{2}}\right) + \begin{pmatrix} 0 \\ g\check{\eta}^+_{i-\frac{1}{2}}\left(\widehat{b}_{i-\frac{1}{2}} - b^+_{i-\frac{1}{2}}\right) \end{pmatrix}. \tag{25}$$

♯ *modified* lowest-order subcell FV fluxes $\left\{\boldsymbol{\mathscr{F}}^{\mathrm{FV},\pm}\right\}_{m\in[\![1,k]\!]}$ and subcell-scale hydrostatic reconstruction: the lowest-order fluxes are now defined relying on *reconstructed mean values* of the bathymetry performed *at the subcell scale* (*i.e.* at subells interfaces). Let us define, for any subcell S_m:

$$\overline{b}_{m-\frac{1}{2}} \coloneqq \max\left(\overline{b}_{m-1}, \overline{b}_m\right), \qquad \overline{b}_{m+\frac{1}{2}} \coloneqq \max\left(\overline{b}_m, \overline{b}_{m+1}\right),$$

together with corresponding reconstructed values for the water-height as follows:

$$\bar{H}^\pm_m \coloneqq \max(0, \bar{\eta}_m - \overline{b}_{m\pm\frac{1}{2}}).$$

Then, for this given subcell, let us define the three intermediate reconstructed values for the bathymetry

$$\begin{aligned} \overline{b}^-_{m+1} &:= \overline{b}_{m+\frac{1}{2}} - \max(0, \overline{b}_{m+\frac{1}{2}} - \bar{\eta}_m), \\ \overline{b}^\pm_m &:= \overline{b}_{m\pm\frac{1}{2}} - \max(0, \overline{b}_{m\pm\frac{1}{2}} - \bar{\eta}_m), \\ \overline{b}^+_{m-1} &:= \overline{b}_{m-\frac{1}{2}} - \max(0, \overline{b}_{m-\frac{1}{2}} - \bar{\eta}_m), \end{aligned}$$

that we assemble with the corresponding three intermediate neighboring reconstructed sub-mean flow-states $\overline{\mathbf{v}}^-_{m-1}, \overline{\mathbf{v}}^+_m, \overline{\mathbf{v}}^-_{m+1}$ defined from reconstructed surface elevation and water-height as follows:

$$\bar{\eta}^-_{m+1} := \bar{H}^-_{m+1} + \overline{b}^-_{m+1}, \quad \bar{\eta}^\pm_m := \bar{H}^\pm_m + \overline{b}^\pm_m, \quad \bar{\eta}^+_{m-1} := \bar{H}^+_{m-1} + \overline{b}^+_{m-1}.$$

The resulting lowest-order fluxes defined upon these reconstructed states are given below:

$$\boldsymbol{\mathscr{F}}^{\mathrm{FV},-}_{m+\frac{1}{2}} := \boldsymbol{\mathscr{F}}\left(\overline{\mathbf{v}}^+_m, \overline{\mathbf{v}}^-_{m+1}, \overline{b}^+_m\right) + \begin{pmatrix} 0 \\ g\overline{\eta}^+_m\left(\overline{b}^+_m - b_h(\widetilde{x}_{m+\frac{1}{2}})\right) \end{pmatrix},$$

$$\boldsymbol{\mathscr{F}}^{\mathrm{FV},+}_{m-\frac{1}{2}} := \boldsymbol{\mathscr{F}}\left(\overline{\mathbf{v}}^+_{m-1}, \overline{\mathbf{v}}^-_m, \overline{b}^-_m\right) + \begin{pmatrix} 0 \\ g\overline{\eta}^-_m\left(\overline{b}^-_m - b_h(\widetilde{x}_{m-\frac{1}{2}})\right) \end{pmatrix}.$$

♯ new *reconstructed* subcell fluxes $\left\{\widehat{\mathbf{F}}^{i,\pm}_{m+\frac{1}{2}}\right\}_{m\in[\![0,k+1]\!]}$: still locally mimicking the behavior of an "in-cell" FV scheme, we obtain the following new expressions for the *reconstructed* subcell fluxes:

$$\widehat{\mathbf{F}}^{i,-}_{m+\frac{1}{2}} \coloneqq \mathbf{F}_h(\widehat{x}^i_{m+\frac{1}{2}}) - C^{i-\frac{1}{2}}_{m+\frac{1}{2}}\left(\mathbf{F}_h(x_{i-\frac{1}{2}}) - \boldsymbol{\mathfrak{F}}^{\mathrm{DG},+}_{i-\frac{1}{2}}\right) - C^{i+\frac{1}{2}}_{m+\frac{1}{2}}\left(\mathbf{F}_h(x_{i+\frac{1}{2}}) - \boldsymbol{\mathfrak{F}}^{\mathrm{DG},-}_{i+\frac{1}{2}}\right), \tag{26}$$

$$\widehat{\mathbf{F}}^{i,+}_{m-\frac{1}{2}} \coloneqq \mathbf{F}_h(\widehat{x}^i_{m-\frac{1}{2}}) - C^{i-\frac{1}{2}}_{m-\frac{1}{2}}\left(\mathbf{F}_h(x_{i-\frac{1}{2}}) - \boldsymbol{\mathfrak{F}}^{\mathrm{DG},+}_{i-\frac{1}{2}}\right) - C^{i+\frac{1}{2}}_{m-\frac{1}{2}}\left(\mathbf{F}_h(x_{i+\frac{1}{2}}) - \boldsymbol{\mathfrak{F}}^{\mathrm{DG},-}_{i+\frac{1}{2}}\right). \tag{27}$$

♯ new *blended* subcell fluxes $\left\{\widetilde{\mathbf{F}}^{i,\pm}_{m+\frac{1}{2}}\right\}_{m\in[\![0,k+1]\!]}$: the *blended* fluxes are naturally introduced as:

$$\widetilde{\mathbf{F}}^{i,-}_{m+\frac{1}{2}} \coloneqq \boldsymbol{\mathfrak{F}}^{\mathrm{FV},-}_{m+\frac{1}{2}} + \Theta_{m+\frac{1}{2}}\left(\widehat{\mathbf{F}}^{i,-}_{m+\frac{1}{2}} - \boldsymbol{\mathfrak{F}}^{\mathrm{FV},-}_{m+\frac{1}{2}}\right), \tag{28}$$

$$\widetilde{\mathbf{F}}^{i,+}_{m-\frac{1}{2}} \coloneqq \boldsymbol{\mathfrak{F}}^{\mathrm{FV},+}_{m-\frac{1}{2}} + \Theta_{m-\frac{1}{2}}\left(\widehat{\mathbf{F}}^{i,+}_{m-\frac{1}{2}} - \boldsymbol{\mathfrak{F}}^{\mathrm{FV},+}_{m-\frac{1}{2}}\right). \tag{29}$$

DG subcell reformulation and monolithic approximation

In order to enforce the well-balancing property for the important class of motionless steady-state solutions, we initially consider the following DG formulation for the NSW equations with bathymetry source term, which relies on the *modified* high-order fluxes (24): for all $\omega_i \in \mathscr{T}_h$, find $\mathbf{v}^i_h(\cdot,t) \coloneqq (\eta^i_h, q^i_h) \in (\mathbb{P}^k(\omega_i))^2$ such that, for all $\varphi \in \mathbb{P}^k(\omega_i)$:

$$\int_{\omega_i} \partial_t \mathbf{v}^i_h \varphi \,\mathrm{d}x - \int_{\omega_i} \mathbf{F}_h \partial_x \varphi \,\mathrm{d}x + \left[\varphi \boldsymbol{\mathfrak{F}}^{\mathrm{DG},\mp}\right]^{i+\frac{1}{2}}_{i-\frac{1}{2}} = \int_{\omega_i} \varphi\, \mathbf{B}_h \,\mathrm{d}x, \tag{30}$$

with interface fluxes shortcut defined as:

$$\left[\varphi \boldsymbol{\mathfrak{F}}^{\mathrm{DG},\mp}\right]^{i+\frac{1}{2}}_{i-\frac{1}{2}} \coloneqq \varphi_{|x_{i+\frac{1}{2}}} \boldsymbol{\mathfrak{F}}^{\mathrm{DG},-}_{i+\frac{1}{2}} - \varphi_{|x_{i-\frac{1}{2}}} \boldsymbol{\mathfrak{F}}^{\mathrm{DG},+}_{i-\frac{1}{2}},$$

and

$$\mathbf{F}_h \coloneqq p^k_h \circ \mathbf{F}(\mathbf{v}_h, b_h), \qquad \mathbf{B}_h \coloneqq p^k_h \circ \mathbf{B}[b_h](\mathbf{v}_h).$$

Let us also define $\overline{\mathbf{B}}_h \coloneqq \overline{\pi}^k_h \mathbf{B}_h$, piecewise constant function associated with the mean-values of B_h on the sub-mesh. Interestingly, such a local modified formulation is still equivalent with a FV-like formulation on the sub-mesh, with a source term computed at the sub-mesh scale:

Proposition 4.1. *For all $\omega_i \in \mathscr{T}_h$, the local DG formulation (30) can be equivalently written as a FV-like scheme defined on the sub-mesh as follows:*

$$\partial_t \overline{\mathbf{v}}^i_m = -\frac{1}{|S^i_m|}\left(\widehat{\mathbf{F}}^{i,-}_{m+\frac{1}{2}} - \widehat{\mathbf{F}}^{i,+}_{m-\frac{1}{2}}\right) + \overline{\mathbf{B}}^i_m, \qquad \forall m \in [\![1, k+1]\!], \tag{31}$$

where $\overline{\mathbf{B}}^i_m = \overline{\mathbf{B}}_{h|S^i_m}$ and the reconstructed fluxes are defined in (26)-(27).

Proof. The proof mainly relies on the definition and use of the so-called sub-resolution basis functions, which are nothing but the L^2 projection of the subcell-indicator functions, *i.e.* $p^k_i \circ \mathbb{1}^i_m$, [40, 80]. □

As in the homogeneous case, the quest for non-linear stability leads to the introduction of a new local subcell FV/DG monolithic approximation, written with a simple first-order time-stepping scheme for the sake of simplicity:

$$\overline{\mathbf{v}}^{i,n+1}_m = \overline{\mathbf{v}}^{i,n}_m - \frac{\Delta t^n}{|S^i_m|}\left(\widetilde{\mathbf{F}}^{i,-}_{m+\frac{1}{2}} - \widetilde{\mathbf{F}}^{i,+}_{m-\frac{1}{2}}\right) + \overline{\mathbf{B}}^i_m, \qquad \forall m \in [\![1, k+1]\!], \qquad \forall i \in [\![1, n_{\mathrm{el}}]\!], \tag{32}$$

where the new *blended* fluxes $\widetilde{\mathbf{F}}^{i,\pm}_{m\pm\frac{1}{2}}$ are defined in (28). Non-linear stability therefore relies on the definition of suitable blended coefficients.

Blended coefficients and water-height non-negativity

An admissible approximate solution is defined with respect to the non-negativity of the sub-mean values:

Definition 4.2. *For any discrete time $n \geq 0$, we say that an approximate state $\mathbf{v}_h(\cdot, t^n) \in (\mathbb{P}^k(\mathscr{T}_h))^2$, or equivalently $\overline{\mathbf{v}}_h^n := \overline{\pi}_h^k \circ \mathbf{v}_h(\cdot, t^n) \in (\mathbb{P}^0(\widetilde{\mathscr{T}_h}))^2$, is admissible if $\overline{\mathbf{v}}_m^{i,n}$ is such that $\overline{\eta}_m^{i,n} - \overline{b}_m^i \geq 0$, for all $\omega_i \in \mathscr{T}_h$ and for all $S_m^i \in \mathscr{T}_{\omega_i}^k$, i.e. $\overline{\mathbf{v}}_m^{i,n} \in \mathscr{H}^+_{\overline{b}_m^i}$:*

A definition of uniquely defined interface-related blending coefficients $\Theta^{\mathscr{H}^+}_{m+\frac{1}{2}}$ that ensures the preservation of water-height non-negativity is provided below:

Proposition 4.3. *Let us consider (32) and assume that $\overline{\mathbf{v}}_h^n$ is admissible, that Δt^n satisfies the CFL-like condition (11) and that the blended-coefficient occurring in (28) satisfies:*

$$\Theta_{m+\frac{1}{2}} \leq \Theta^{\mathscr{H}^+}_{m+\frac{1}{2}} := \min\left(\Theta^{\mathscr{H}^+,-}_{m+\frac{1}{2}}, \Theta^{\mathscr{H}^+,+}_{m+\frac{1}{2}}\right), \tag{33}$$

with

$$\Theta^{\mathscr{H}^+,-}_{m+\frac{1}{2}} \leq \begin{cases} \dfrac{\sigma\left(\eta^{*,-}_{m+\frac{1}{2}} - \overline{b}_m\right)}{\Delta\mathbf{F}^{(1),-}_{m+\frac{1}{2}}} & \text{if } \Delta\mathbf{F}^{(1),-}_{m+\frac{1}{2}} > 0, \\ 1 & \text{else,} \end{cases} \qquad \Theta^{\mathscr{H}^+,+}_{m+\frac{1}{2}} \leq \begin{cases} \dfrac{\sigma\left(\overline{b}_{m+1} - \eta^{*,+}_{m+\frac{1}{2}}\right)}{\Delta\mathbf{F}^{(1),+}_{m+\frac{1}{2}}} & \text{if } \Delta\mathbf{F}^{(1),+}_{m+\frac{1}{2}} < 0, \\ 1 & \text{else,} \end{cases}$$

where we set $\Delta\mathbf{F}^{(1),\pm}_{m+\frac{1}{2}} := \widehat{\mathbf{F}}^{\pm,(1)}_{m+\frac{1}{2}} - \boldsymbol{\mathfrak{F}}^{\mathrm{FV},\pm,(1)}_{m+\frac{1}{2}}$. Then $\overline{\mathbf{v}}_h^{n+1}$ is admissible.

Proof. The proof is quite similar to the one of Proposition 3.3, ensuring that the inequalities

$$\eta^{*,-}_{m+\frac{1}{2}} - \frac{\widehat{\mathbf{F}}^{-,(1)}_{m+\frac{1}{2}} - \boldsymbol{\mathfrak{F}}^{\mathrm{FV},-,(1)}_{m+\frac{1}{2}}}{\sigma} \geq \overline{b}_m \qquad \text{and} \qquad \eta^{*,+}_{m+\frac{1}{2}} + \frac{\widehat{\mathbf{F}}^{+,(1)}_{m+\frac{1}{2}} - \boldsymbol{\mathfrak{F}}^{\mathrm{FV},+,(1)}_{m+\frac{1}{2}}}{\sigma} \geq \overline{b}_{m+1},$$

are uniformly satisfied. Let us remark that this is ensured only if the 1^{st}-order Riemann intermediate states are also preserving water-height positivity at the discrete level, *i.e.* if $\eta^{*,-}_{m+\frac{1}{2}} \geq \overline{b}_m$ and $\eta^{*,+}_{m+\frac{1}{2}} \geq \overline{b}_{m+1}$, which is demonstrated in Appendix A. □

Remark 4.4. *In practice, one set $\Theta_{m+\frac{1}{2}} := \min\left(\Theta^{\mathscr{H}^+}_{m+\frac{1}{2}}, \Theta^{\mathrm{sNAD}}_{m+\frac{1}{2}}\right)$ to ensure both water-height non-negativity and control of oscillations near singularities for the NSW equations.*

Consistency between source term and initial-data approximations

After Proposition 4.3, it appears that the approximate initial-data $\mathbf{v}_h^0$ has to be admissible in order to initiate a sequence of admissible approximate states, relying on the suitable CFL-condition and blended-coefficients. Hence, starting from some physical or idealized (analytical) initial-condition $\mathbf{v}^0 := (\eta^0, q^0)$ and bathymetry parameterization b such that $\eta^0 - b \geq 0$, we observe that $\widetilde{\pi}_h^k(\eta^0 - b) \geq 0$, hence $\overline{\mathbf{v}}_h^0 := \widetilde{\pi}_h^k \mathbf{v}^0$ is admissible. In an equivalent way, we also have that $\mathbf{v}_h^0 := (\overline{\pi}_h^k)^{-1}\overline{\mathbf{v}}_h^0$ is admissible. From this last formula, we observe that the initial approximate surface-elevation has to be defined is a consistent way with the previous definition of the approximate bathymetry:

$$\eta_h^0 := (\overline{\pi}_h^k)^{-1}\widetilde{\pi}_h^k \eta^0 - b_h. \tag{34}$$

Let us also emphasize that when initializing with some data corresponding to a motionless steady-state $\mathbf{v}_h = (\eta_h, q_h) := (\eta^e, 0)$, then $\mathbf{F}(\mathbf{v}_h, b_h)$ belongs to $(\mathbb{P}^k(\mathscr{T}_h))^2$ and as a consequence, we have:

$$\mathbf{F}_h := p_h^k \circ \mathbf{F}(\mathbf{v}_h, b_h) = \mathbf{F}(\mathbf{v}_h, b_h).$$

In a similar way, we also have $\mathbf{B}_h := \mathbf{B}[b_h](\mathbf{v}_h)$.

Motionless steady-states preservation

Proposition 4.5. *The discrete formulation (32) preserves the motionless steady states:*

$$\forall n \in \mathbb{N}, \qquad (\eta_h^n = \eta^e \text{ and } q_h^n = 0) \Longrightarrow \left(\eta_h^{n+1} = \eta^e \text{ and } q_h^{n+1} = 0\right).$$

Proof. Let us rewrite the FV-like scheme as follows:

$$\begin{aligned}\overline{\mathbf{v}}_m^{i,n+1} = \overline{\mathbf{v}}_m^{i,n} - \frac{\Delta t^n}{|S_m^i|}(&\boldsymbol{\mathfrak{F}}_{m+\frac{1}{2}}^{i,n,-} + \Theta_{m+\frac{1}{2}}^{i,n}\left(\widehat{\mathbf{F}}_{m+\frac{1}{2}}^{i,n,-} - \boldsymbol{\mathfrak{F}}_{m+\frac{1}{2}}^{i,n,-}\right) - \\ &\boldsymbol{\mathfrak{F}}_{m-\frac{1}{2}}^{i,n,+} + \Theta_{m-\frac{1}{2}}^{i,n}\left(\widehat{\mathbf{F}}_{m-\frac{1}{2}}^{i,n,+} - \boldsymbol{\mathfrak{F}}_{m-\frac{1}{2}}^{i,n,+}\right)) + \Delta t^n \overline{\mathbf{B}}_m^{i,n}. \end{aligned} \tag{35}$$

If one considers the case $\Theta_{m+\frac{1}{2}}^{i,n} = \Theta_{m-\frac{1}{2}}^{i,n} = 1$, then the monolithic scheme is equivalent to a DG scheme in its subcell formulation:

$$\overline{\mathbf{v}}_m^{i,n+1} = \overline{\mathbf{v}}_m^{i,n} - \frac{\Delta t^n}{|S_m^i|}\left(\widehat{\mathbf{F}}_{m+\frac{1}{2}}^{i,n} - \widehat{\mathbf{F}}_{m-\frac{1}{2}}^{i,n}\right) + \Delta t^n \overline{\mathbf{B}}_m^i.$$

Dropping the (i,n) superscripts for clarity, at the cell scale and at steady-state, the following identities are satisfied:

$$\eta_{i\pm\frac{1}{2}}^+ = \eta_{i\pm\frac{1}{2}}^- = \eta^e, \qquad q_{i\pm\frac{1}{2}}^+ = q_{i\pm\frac{1}{2}}^- = 0, \qquad b_{i\pm\frac{1}{2}}^+ = b_{i\pm\frac{1}{2}}^-.$$

Then the high-order numerical flux on cells $\boldsymbol{\mathfrak{F}}^{\mathrm{DG},\pm}$ verifies

$$\boldsymbol{\mathfrak{F}}_{i\pm\frac{1}{2}}^{\mathrm{DG},\mp} = \mathbf{F}\left(\mathbf{v}_h(x_{i\pm\frac{1}{2}}), b_h(x_{i\pm\frac{1}{2}})\right),$$

such that

$$\widehat{\mathbf{F}}_{m\pm\frac{1}{2}}^{\mp} = \mathbf{F}\left(\mathbf{v}_h(\widetilde{x}_{m\pm\frac{1}{2}}), b_h(\widetilde{x}_{m\pm\frac{1}{2}})\right).$$

Consequently we get:

$$\widehat{\mathbf{F}}_{m+\frac{1}{2}}^{-} - \widehat{\mathbf{F}}_{m-\frac{1}{2}}^{+} = \int_{S_m} \partial_x \mathbf{F}\left(\mathbf{v}_h, b_h\right) \,\mathrm{d}x,$$

and we finally have

$$\overline{\mathbf{v}}_m^{i,n+1} = \overline{\mathbf{v}}_m^{i,n} - \frac{\Delta t^n}{|S_m^i|}\int_{S_m^i} \partial_x \mathbf{F}\left(\mathbf{v}_h, b_h\right) \,\mathrm{d}x + \frac{\Delta t^n}{|S_m^i|}\int_{S_m^i} \mathbf{B}(\mathbf{v}_h, \partial_x b_h)\,\mathrm{d}x = \overline{\mathbf{v}}_m^{i,n}.$$

If we consider the first-order case, *i.e.* $\Theta_{m+\frac{1}{2}}^{i,n} = \Theta_{m-\frac{1}{2}}^{i,n} = 0$, we get the following first-order scheme with subcell FV fluxes:

$$\overline{\mathbf{v}}_m^{i,n+1} = \overline{\mathbf{v}}_m^{i,n} - \frac{\Delta t^n}{|S_m^i|}\left(\boldsymbol{\mathfrak{F}}_{m+\frac{1}{2}}^{i,n,-} - \boldsymbol{\mathfrak{F}}_{m-\frac{1}{2}}^{i,n,+}\right) + \Delta t^n \overline{\mathbf{B}}_m^i.$$

At the subcell scale, we also have at steady state: $\overline{\eta}_m^+ = \overline{\eta}_{m+1}^- = \eta^e$ and $\overline{q}_m^+ = \overline{q}_{m+1}^- = 0$, leading to

$$\begin{aligned}\boldsymbol{\mathfrak{F}}\left(\overline{\mathbf{v}}_m^+, \overline{\mathbf{v}}_{m+1}^-, \overline{b}_m^+\right) &= \frac{1}{2}\left(\mathbf{F}\left(\overline{\mathbf{v}}_m^+, \overline{b}_m^+\right) + \mathbf{F}\left(\overline{\mathbf{v}}_{m+1}^-, \overline{b}_m^+\right)\right) - \frac{\sigma}{2}\left(\overline{\mathbf{v}}_{m+1}^- - \overline{\mathbf{v}}_m^+\right) \\ &= \frac{1}{2}\left(\mathbf{F}\left(\overline{\mathbf{v}}_m^+, \overline{b}_m^+\right) + \mathbf{F}\left(\overline{\mathbf{v}}_{m+1}^-, \overline{b}_m^+\right)\right) \\ &= \frac{1}{2}\begin{pmatrix} 0 \\ g\left((\eta^e)^2 - 2\eta^e \overline{b}_m^+\right)\end{pmatrix},\end{aligned}$$

and then to:

$$\begin{aligned}\boldsymbol{\mathfrak{F}}_{m+\frac{1}{2}}^{-} &= \frac{1}{2}\begin{pmatrix} 0 \\ g\left((\eta^e)^2 - 2\eta^e \overline{b}_m^+\right)\end{pmatrix} + \begin{pmatrix} 0 \\ g\overline{\eta}_m^+\left(\overline{b}_m^+ - 2\eta^e b_h(\widetilde{x}_{m+\frac{1}{2}})\right)\end{pmatrix} = \frac{1}{2}\begin{pmatrix} 0 \\ g\left((\eta^e)^2 - 2\eta^e b_h(\widetilde{x}_{m+\frac{1}{2}})\right)\end{pmatrix} \\ &= \mathbf{F}\left(\mathbf{v}_h(\widetilde{x}_{m+\frac{1}{2}}), b_h(\widetilde{x}_{m+\frac{1}{2}})\right),\end{aligned}$$

and in a similar way

$$\boldsymbol{\mathcal{F}}^{+}_{m-\frac{1}{2}} = \mathbf{F}\left(\mathbf{v}_h(\widetilde{x}_{m-\frac{1}{2}}), b_h(\widetilde{x}_{m-\frac{1}{2}})\right).$$

It is then easy to see, as previously, that the fluxes are cancelling the source term exactly:

$$\overline{\mathbf{v}}_m^{i,n+1} = \overline{\mathbf{v}}_m^{i,n} - \frac{\Delta t^n}{|S_m^i|}\int_{S_m^i} \partial_x \mathbf{F}\left(\mathbf{v}_h, b_h\right)\,\mathrm{d}x + \frac{\Delta t^n}{|S_m^i|}\int_{S_m^i} \mathbf{B}(\mathbf{v}_h, \partial_x b_h)\,\mathrm{d}x = \overline{\mathbf{v}}_m^{i,n}.$$

If we now consider the more general case where $\left(\Theta^{i,n}_{m-\frac{1}{2}}, \Theta^{i,n}_{m+\frac{1}{2}}\right) \in [0,1]^2$, the following identities are still satisfied:

$$\begin{cases} \boldsymbol{\mathcal{F}}^{i,n,\mp}_{m\pm\frac{1}{2}} = \mathbf{F}\left(\mathbf{v}_h(\widetilde{x}_{m\pm\frac{1}{2}}), b_h(\widetilde{x}_{m\pm\frac{1}{2}})\right), \\ \widehat{\mathbf{F}}^{i,n,\mp}_{m\pm\frac{1}{2}} = \mathbf{F}\left(\mathbf{v}_h(\widetilde{x}_{m\pm\frac{1}{2}}), b_h(\widetilde{x}_{m\pm\frac{1}{2}})\right). \end{cases}$$

leading to $\widehat{\mathbf{F}}^{i,n,\mp}_{m\pm\frac{1}{2}} = \boldsymbol{\mathcal{F}}^{i,n,\mp}_{m\pm\frac{1}{2}}$ at steady-state. We finally get

$$\begin{aligned}
\overline{\mathbf{v}}_m^{i,n+1} &= \overline{\mathbf{v}}_m^{i,n} - \frac{\Delta t^n}{|S_m^i|}\left(\boldsymbol{\mathcal{F}}^{i,n,-}_{m+\frac{1}{2}} - \boldsymbol{\mathcal{F}}^{i,n,+}_{m-\frac{1}{2}} + \Theta^{i,n}_{m+\frac{1}{2}}\left(\widehat{\mathbf{F}}^{i,n,-}_{m+\frac{1}{2}} - \boldsymbol{\mathcal{F}}^{i,n,-}_{m+\frac{1}{2}}\right) - \Theta^{i,n}_{m-\frac{1}{2}}\left(\widehat{\mathbf{F}}^{i,n,+}_{m-\frac{1}{2}} - \boldsymbol{\mathcal{F}}^{i,n,+}_{m-\frac{1}{2}}\right)\right) + \Delta t^n \overline{\mathbf{B}}^{i,n}_m \\
&= \overline{\mathbf{v}}_m^{i,n} - \frac{\Delta t^n}{|S_m^i|}\left(\mathbf{F}\left(\mathbf{v}_h(\widetilde{x}_{m+\frac{1}{2}}), b_h(\widetilde{x}_{m+\frac{1}{2}})\right) - \mathbf{F}\left(\mathbf{v}_h(\widetilde{x}_{m-\frac{1}{2}}), b_h(\widetilde{x}_{m-\frac{1}{2}})\right)\right) + \Delta t^n \overline{\mathbf{B}}^{i,n}_m \\
&= \overline{\mathbf{v}}_m^{i,n} - \frac{\Delta t^n}{|S_m^i|}\int_{S_m^i} \partial_x \mathbf{F}\left(\mathbf{v}_h, b_h\right)\,\mathrm{d}x + \frac{\Delta t^n}{|S_m^i|}\int_{S_m^i} \mathbf{B}(\mathbf{v}_h, \partial_x b_h)\,\mathrm{d}x \\
&= \overline{\mathbf{v}}_m^{i,n}.
\end{aligned}$$

□

4.2. Higher-order differential source terms and weakly dispersive models

Let us consider the GN equations (4)-(6):

$$\partial_t \mathbf{v} + \partial_x \mathbf{F}(\mathbf{v}, b) = \mathbf{B}[b](\mathbf{v}) + \mathbf{D}[H](\mathbf{v}, \Lambda), \tag{36}$$

$$\mathscr{L}[H, b]\Lambda = \mathbb{Q}[H, b](\mathbf{v}), \tag{37}$$

where $\mathbf{D}$ is defined in (5), $\mathscr{L}[H,b]$ and $\mathbb{Q}[H,b](\mathbf{v})$ respectively in (7) and (3). As previously recalled, several weakly-dispersive shallow water model may fall in this formalism and we focus on the GN equations as an example. The initial DG formulation associated with (36)-(37) reads as follows: find $(\mathbf{v}_h, \Lambda_h) \in (\mathbb{P}^k(\mathscr{T}_h))^3$ such that for all $(\phi, \varphi) \in (\mathbb{P}^k(\mathscr{T}_h))^2$,

$$\sum_{\omega_i \in \mathscr{T}_h}\int_{\omega_i} \partial_t \mathbf{v}_h \varphi\,\mathrm{d}x = \sum_{\omega_i \in \mathscr{T}_h}\left(\int_{\omega_i} \mathbf{F}_h \partial_x \varphi\,\mathrm{d}x - \left[\varphi \boldsymbol{\mathcal{F}}^{\mathrm{DG},\mp}\right]_{i-\frac{1}{2}}^{i+\frac{1}{2}} + \int_{\omega_i} \mathbf{B}_h \varphi\,\mathrm{d}x + \int_{\omega_i} p_i^k \circ \mathbf{D}[H_h](\mathbf{v}_h, \Lambda_h)\varphi\,\mathrm{d}x\right), \tag{38}$$

$$\mathscr{L}_h(\Lambda_h, \phi) = \sum_{\omega_i \in \mathscr{T}_h}\int_{\omega_i} Q_h(\mathbf{v}_h)\phi\,\mathrm{d}x, \tag{39}$$

where the definition of the discrete bilinear form $\mathscr{L}_h$, which is consistent with $\mathscr{L}[H,b]$, symmetric and coercive (providing that some penalty coefficient is large enough) and the computation of Q_h, discrete counterpart of $\mathbb{Q}[H,b](\mathbf{v})$, are directly borrowed from [86]. We emphasize that the regularizing effect of the operator $\mathscr{L}[H,b]$ allows to consider some (possibly non-conforming) high-order methods to approximate the solution of such an elliptic problem, and expect to observe some high-order convergence. We also highlight that from a numerical viewpoint, the discrete bilinear form $(\mathbb{P}^k(\mathscr{T}_h))^2 \ni (\phi_h, \psi_h) \mapsto \mathscr{L}_h(\phi_h, \psi_h)$ introduced in [86] may be regarded as an Interior Penalty discontinuous Galerkin (SIP-DG) method, designed for some heterogeneous and discontinuous coefficients, and taking advantages of the particular structure of the underlying operator $(1 + \mathscr{T}[H,b])$. The resulting formulation belongs to the family of Symmetric Weighted IP (SWIP) methods and is recalled in Appendix C. The computation of Q_h is performed using an integration-collocation method, see [22] for the complete description, which is not recalled here.

A combined local subcell monolithic DG/FV - SWIP-DG method

Following the lines of the previous sections, one can show that the high-order DG method (38) associated with a first-order time-marching method, is equivalent to the following "in-cell" FV-like scheme: find $(\overline{\mathbf{v}}_h^{n+1}, \Lambda_h^n) \in (\mathbb{P}^0(\widetilde{\mathscr{T}_h}))^2 \times \mathbb{P}^k(\mathscr{T}_h)$ such that

$$\overline{\mathbf{v}}_m^{i,n+1} = \overline{\mathbf{v}}_m^{i,n} - \frac{\Delta t^n}{|S_m^i|}\left(\widehat{\mathbf{F}}^{i,-}_{m+\frac{1}{2}} - \widehat{\mathbf{F}}^{i,+}_{m-\frac{1}{2}}\right) + \Delta t^n\left(\overline{\mathbf{B}}_m^i + \overline{\mathbf{D}}_m^i\right), \qquad \forall \omega_i \in \mathscr{T}_h, \ \ \forall m \in [\![1, k+1]\!], \tag{40}$$

$$\overline{\mathbf{D}}_m^i := \overline{\mathbf{D}}^i_{h|S_m^i}, \quad \text{with} \quad \overline{\mathbf{D}}_h^i := \overline{\pi}_i^k \circ p_i^k \circ \mathbf{D}[H_h^n](\mathbf{v}_h^n, \Lambda_h^n)_{|\omega_i}, \qquad \forall \omega_i \in \mathscr{T}_h, \ \ \forall m \in [\![1, k+1]\!], \tag{41}$$

$$\mathscr{L}_h(\Lambda_h^n, \phi) = \sum_{\omega_i \in \mathscr{T}_h} \int_{\omega_i} Q_h(\mathbf{v}_h^n)\phi \, \mathrm{d}x, \qquad \forall \phi \in \mathbb{P}^k(\mathscr{T}_h), \tag{42}$$

where the reconstructed fluxes $\left\{\widehat{\mathbf{F}}^{i,\mp}_{m\pm\frac{1}{2}}\right\}_{m\in[\![0,k+1]\!]}$ are still defined as before.

From this, it is of course natural to introduce a new combined local subcell monolithic DG/FV - SWIP-DG fully-discrete counterpart of (40)-(41)-(42), as follows: find $(\overline{\mathbf{v}}_h^{n+1}, \Lambda_h^n) \in (\mathbb{P}^0(\widetilde{\mathscr{T}_h}))^2 \times \mathbb{P}^k(\mathscr{T}_h)$ such that

$$\overline{\mathbf{v}}_m^{i,n+1} = \overline{\mathbf{v}}_m^{i,n} - \frac{\Delta t^n}{|S_m^i|}\left(\widetilde{\mathbf{F}}^{i,-}_{m+\frac{1}{2}} - \widetilde{\mathbf{F}}^{i,+}_{m-\frac{1}{2}}\right) + \Delta t^n\left(\overline{\mathbf{B}}_m^i + \overline{\mathbf{D}}_m^i\right), \qquad \forall \omega_i \in \mathscr{T}_h, \ \ \forall m \in [\![1, k+1]\!], \tag{43}$$

supplemented with (41)-(42) where the blended fluxes $\left\{\widetilde{\mathbf{F}}^{i,\mp}_{m\pm\frac{1}{2}}\right\}_{m\in[\![0,k+1]\!]}$, and the associated blended coefficients are still defined as above.

Remark 4.6. *From a practical viewpoint, let us consider a "classical" DG numerical implementation in which, for any given mesh element ω_i, the dispersive contributions to the residuals in the momentum balance law (38)*

$$\mathbf{D}\mathbf{\Psi}_h^i := \left(\int_{\omega_i} \mathbf{D}_h^i \psi_j^i \, \mathrm{d}x\right)_{j\in[\![1,k+1]\!]} \in \mathbb{R}^{k+1}$$

are available. Then, we have the following identity:

$$\overline{\mathbf{D}}_h^i = \mathbb{P}_i \mathbb{M}_i^{-1} \mathbf{D}\mathbf{\Psi}_h^i,$$

where $\mathbb{P}_i$ is the projection matrix introduced in Remark 2.5 and $\mathbb{M}_i$ is the mass-matrix associated with the element ω_i and the set of basis function (8).

Remark 4.7. *Several properties, including the preservation of the water-height non-negativity and the preservation of motionless steady-states, are straightforwardly inherited from the discretization of the NSW equations. In particular, the dispersive contributions to the momentum balance equation vanishes with respect to the velocity, making the preservation of the steady-states directly related to the well-posedness of the discrete elliptic problems $\mathscr{L}_h(\Lambda_h^n, \phi) = 0$. We refer the interested reader to [57].*

5. Numerical validations

In the following, we apply the local subcell monolithic DG/FV methods of the previous section to several examples which aim at validating various assets of the proposed approximation method, involving the hyperbolic NSW equations (32), and also the dispersive GN shallow-water equations (40)-(41)-(42) for the last two tests. If not stated otherwise, we define the blended fluxes according to Remark (4.4). We recall that globally setting $\Theta = 1$ in (28) allows to recover the classical DG method.

5.1. Smooth sinusoidal solutions

Periodic solution

Simulation parameters.

Computational domain: $\Omega = [0, 1]$
Number of cells: $n_{\text{el}} = 50$ cells
Boundary conditions: periodic

Polynomial degree: $k = 1, 2, 3$
Time-marching order: $p = 3$
Final time: $t_{\max} = 0.3,\ 0.6$ sec

The goal of this first test is the assessment of some convergence properties in L^2-norm of the proposed monolithic DG-FV scheme. We follow the lines of [83] and [40] to generate a family of smooth solutions for the homogeneous NSW equations, considering the following initial data:

$$\eta_0 = \frac{u_0^2}{4g} \quad \text{and} \quad q_0 = \frac{u_0^3}{4g},$$

where the initial constant velocity is defined as follows:

$$u_0(x) := 1 + 0.1\sin(2\pi x).$$

We compute the time-evolution of this initial profile up to $t_{\max} = 0.6\,s$ and we compare the adequacy between the numerical results and the corresponding exact solution for increasing approximating polynomial's degrees. As an example, a snapshot of the free-surface elevation is shown on Fig. 4 (left) for $k = 3$.

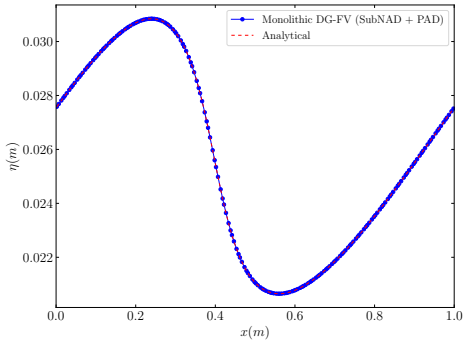

k	1		2		3	
h	$E^{\eta}_{L^2}$	$r^{\eta}_{L^2}$	$E^{\eta}_{L^2}$	$r^{\eta}_{L^2}$	$E^{\eta}_{L^2}$	$r^{\eta}_{L^2}$
0.025	6.11E-6	2.03	1.49E-7	3.01	2.57E-9	3.98
0.012	1.47E-6	2.01	1.77E-8	3.00	1.56E-10	4.01
0.009	3.64E-7	2.01	5.09E-9	3.00	3.05E-11	4.00
0.006	1.64E-7	–	2.10E-9	–	9.60E-12	–

Figure 4: Test 1 - Periodic sinusoidal solution - Free-surface elevation at $t_f = 0.3\,s$ for $k = 3$ (left) and L^2-errors between numerical and exact solutions with associated convergence rates for η.

We also compute the global L^2-errors for the free-surface elevation η for increasing polynomial's degree and increasingly refined meshes. These errors are gathered in the Table associated with Fig. 4 (right) and we deduce the related numerical convergence-rates, which scale as $O(k+1)$. Although not shown here, similar behaviors are observed for the approximation of the horizontal discharge q.

With a dry area

Simulation parameters.

Computational domain: $\Omega = [0, 1]$
Number of cells: $n_{\text{el}} = 10$ cells
Boundary conditions: homogeneous Neumann

Polynomial degree: $k = 8$
Time-marching order: $p = 3$
Final time: $t_{\max} = 0.09$ sec

In order to investigate the discrete preservation of the water-height positivity, and following a similar process, we consider the initial velocity profile:

$$u_0(x) := \begin{cases} 2 & \text{if } x \leq \frac{1}{4}, \\ 1 + \sin(2\pi x) & \text{if } x \in \left[\frac{1}{4}, \frac{3}{4}\right], \\ 0 & \text{else.} \end{cases}$$

The computation is performed for a very high polynomial degree ($k = 8$) and a very coarse mesh ($n_{\text{el}} = 10$) up to $t_{\max} = 0.09\,s$ and we show the corresponding free-surface on Fig. 5 (left), with a zoom on the wet-dry transition (right). Note that the vertical light-grey lines help to visualize the mesh cells boundaries, while the blue-dots are associated with subcell mean-values inside the mesh cells (we recall that the subcells spatial distribution is not uniform for accuracy issues). This second situation highlights a highly enjoyable robustness property, even with the use of a very low grid-resolution and a high-order polynomial approximation, a combination that is generally prone to oscillations and fast propagating instabilities. We also observe an accurate front propagation's speed as emphasized by the visual comparison with the corresponding exact solution.

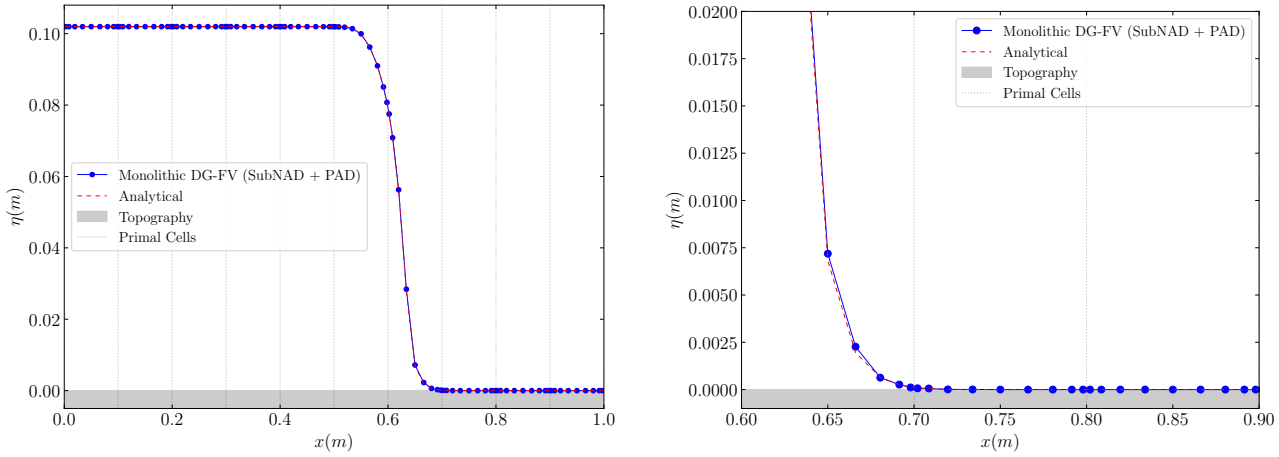

Figure 5: Test 1 - Sinusoidal solution on dry bed - Free surface elevation computed at $t_{\max} = 0.09\,s$ for $k = 8$ and $n_{\text{el}} = 10$ (left), with a zoom on the wet-dry transition (right).

5.2. Dam-breaks

Shock-waves generation and propagation are unavoidable benchmarks for any nonlinear hyperbolic model and in the context of shallow-water equations, we particularly focus on the efficiency of the proposed stabilization mechanisms for higher-order approximations of bore propagation (relaxed subNAD), and the robustness in the vicinity of the wet-dry interface when the dam-break simulation involves the flooding of initially dry areas (PAD).

Dam-break with uniformly wet-bed

Simulation parameters.

Computational domain: $\Omega = [0, 1]$
Number of cells: $n_{\text{el}} = 50, 10$ cells
Boundary conditions: homogeneous Neumann

Polynomial degree: $k = 3, 9$
Time-marching order: $p = 3$
Final time: $t_{\max} = 0.075$ sec

We now shed our attention to the following initial data:

$$\eta_0(x) = \begin{cases} 1 & \text{if } x \leq 0.5, \\ 0.5 & \text{else,} \end{cases} \qquad q_0 = 0, \qquad b = 0,$$

in order to assess the ability of our method to handle discontinuities with very high-order polynomial approximations in a robust and stable way. We performed an extensive collection of computations involving various combinations of polynomial degrees and mesh refinements and we choose to show the numerical results associated with the following two combinations: $k = 3$ / $n_{\text{el}} = 50$, and $k = 9$ / $n_{\text{el}} = 10$ and the corresponding free-surface profiles on Fig. 6 (note that the light-grey vertical lines are only plotted for the second combination $n_{\text{el}} = 10$ for readability purpose). We observe a very sharp resolution of the discontinuities in both cases, and we emphasize that the shock-wave and the rarefaction-fan are respectively very accurately captured in the middle of only one large mesh element for the second configuration, thanks to the subcell resolution of the method. Of course, we recall that the standard DG methods with high-order elements will not lead to any kind of suitable approximation, since over and undershoots are quickly amplified and the simulations aborted.

Dam-break with flooding

Simulation parameters.

Computational domain: $\Omega = [0, 1]$
Number of cells: $n_{\text{el}} = 50$ cells
Boundary conditions: homogeneous Neumann

Polynomial degree: $k = 3$
Time-marching order: $p = 3$
Final time: $t_{\max} = 0.05$ sec

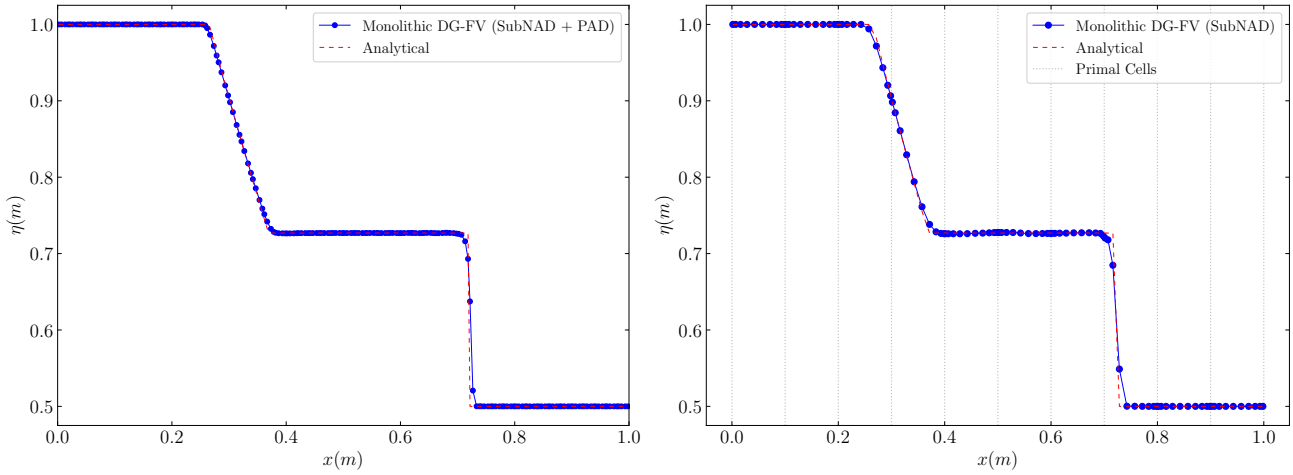

Figure 6: Test 2 - Dam-break - Free surface elevation computed at $t_{\max} = 0.075\,s$ for $k = 3$ / $n_{\text{el}} = 50$ (left) and $k = 9$ / $n_{\text{el}} = 10$ (right).

A similar computation is also performed with the following initial condition involving a uniformly dry-area on the right part of the computational domain:

$$\eta_0(x) = \begin{cases} 1 & \text{if } x \leq 0.5, \\ 0 & \text{else,} \end{cases} \qquad q_0 = 0, \qquad b = 0,$$

in order to highlight the robustness of the method. We show on Fig. 7 (left) some free-surface elevation profiles at various discrete times along the interval $[0.005\,s, 0.05\,s]$, with a zoom (right) highlighting the accurate resolution of the wet-dry front location.

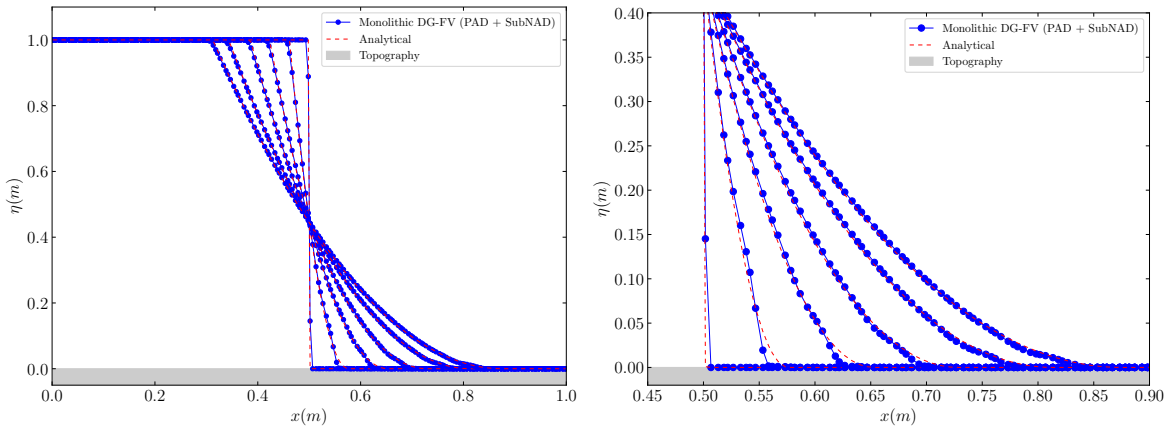

Figure 7: Test 2 - Dam-break with flooding - Free surface elevation at various times in the interval $[0.005, 0.05]$, for $k = 3$ and $n_{\text{el}} = 50$.

5.3. Preservation of motionless steady-states

Simulation parameters.

Computational domain: $\Omega = [0, 1000]$
Number of cells: $n_{\text{el}} = 100$ cells
Boundary conditions: solid wall

Polynomial degree: $k = 3$
Time-marching order: $p = 1$
Final time: $t_{\max} = 500$ sec

In this third test-case, we focus on the ability of the method to preserve motionless steady states, with possibly discontinous topography, and for arbitrary approximating polynomial's degree. We consider the following

topography profile:

$$b(x) = \begin{cases} A\left(\sin\left(\dfrac{(x-x_1)\cdot\pi}{750}\right)\right)^2 & \text{if } x_1 \leq x < x_2, \\ 5 & \text{if } x_2 \leq x < x_3, \\ 0 & \text{elsewhere,} \end{cases}$$

with $x_1 = 125$, $x_2 = 500$, $x_3 = 750$ and $A = 8.75$, combining smooth and discontinuous variations. Two different initial-data are considered: (i) $\eta_0 \coloneqq 10$ (fully immersed bathymetry, see Fig. 8, (ii) $\eta_0 \coloneqq 4$ (semi-immersed bathymetry, see Fig. 9, and $q_0 \coloneqq 0$ in both cases. We assess an accurate preservation of such motionless steady-states through the computation of the L^2 errors between the resulting free-surface and discharge at $T_f = 500\,s$ and the initial-data. We observe that such errors vanish up to double-precision accuracy for the first configuration (fully immersed topography).

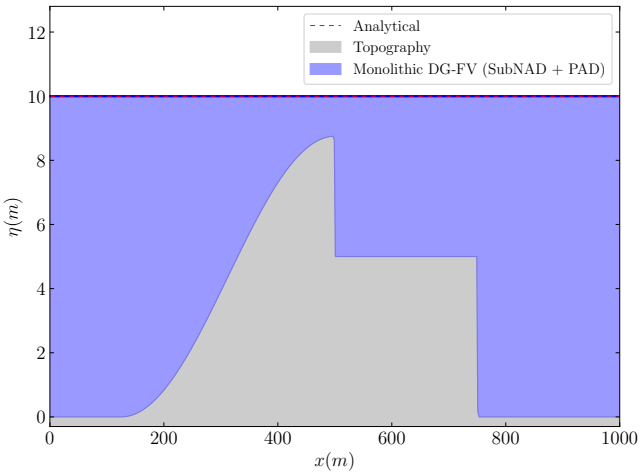

Figure 8: Test 3 - Preservation of a motionless steady state (first case) - Free surface elevation computed at $t_{\max} = 500$ sec, for $k = 3$ and $n_{\text{el}} = 100$.

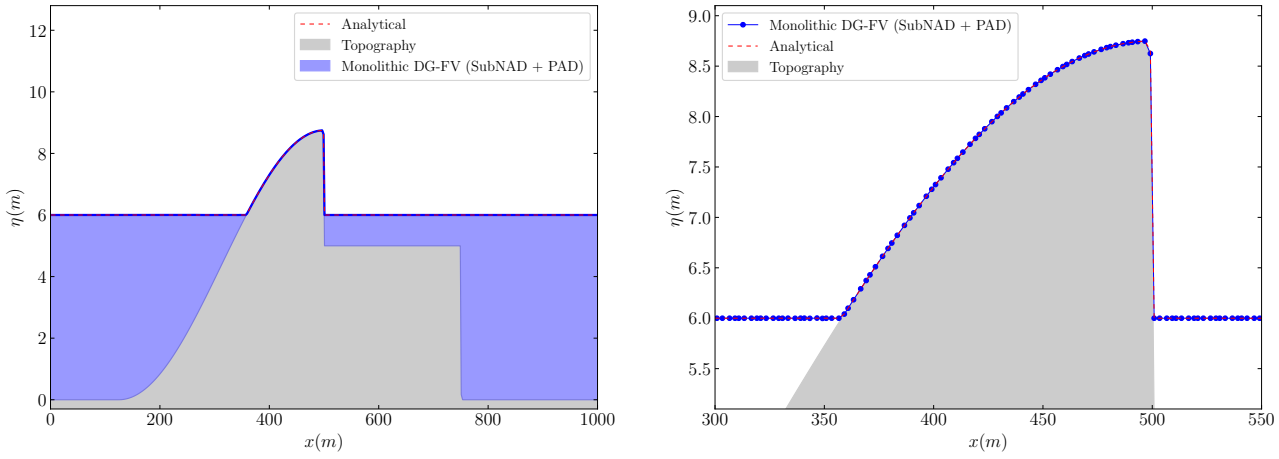

Figure 9: Test 3 - Preservation of a motionless steady state (second case) - Free surface elevation computed at $t_{\max} = 500$ sec, for $k = 3$ and $n_{\text{el}} = 100$, with a zoom on dry structure.

5.4. Carrier & Greenspan's solutions

The fourth test-case is devoted to the study of the so-called *Carrier & Greenspan* solutions for the NSW equations with varying topography, see [13]. These solutions focus on wave's behavior on sloping beaches,

giving access to time histories of specific wave-forms and exhibiting time-evolving wet-dry interfaces over uneven topography: they are therefore frequently used to assess the ability of numerical methods to compute such evolutions over larger computational times, as this is a very challenging problem for high-order methods (small water-heights occur and thus small undershoots may lead to very large relative undershoots).Two solutions are investigated: the first one involves a transient motion asymptotically converging toward a flat free surface, settling toward the mean sea-level in a continuous way, while the second one involves periodic oscillations with free-surface inflexions and velocity reversals at the shoreline. Note that both evolutions are time-driven by the left non-homogeneous Dirichlet boundary-conditions.

Transient C&G solution

Simulation parameters.

Computational domain: $\Omega = [-20, 6]$
Number of cells: $n_{\text{el}} = 50, 10$ cells
Boundary conditions: Dirichlet (left) & homogeneous Neumann (right)

Polynomial degree: $k = 3, 8$
Time-marching order: $p = 1$
Final time: $t_{\max} = 30$ sec

In the so-called *transient C&G* solution, the free-surface is initially depressed near the shoreline, and held motionless before being released at $t = 0$, generating a surging wave that travels up the beach and asymptotically converges towards an equilibrium state. This is therefore a valuable benchmark in the process of evaluating the robustness of the monolithic DG-FV scheme for the computation of long-waves run-up and the ability to converge towards (quasi-)steady-states. To compare the numerical approximations with the exact values of the solutions, denoting by l be the typical length scale of the wave and α the topography slope, we introduce the following nondimensionalized coordinates:

$$x^* = x/l, \quad \eta^* = \eta/(\alpha l), \quad u^* = u/\sqrt{g\alpha l}, \quad t^* = t/\sqrt{l/\alpha g}, \quad c^* = \sqrt{\eta^* - x^*}, \tag{44}$$

and follow the path of [13] with a classical hodograph transformation relying on two dimensionless variables σ^* and λ^*, respectively emulating space and time-like coordinates, and defined as follows:

$$\sigma^* = 4c^* \quad \text{and} \quad \lambda^* = 2\left(u^* + t^*\right).$$

This transformation allows to formulate the initial-data in a closed-form:

$$\eta_0^*(\sigma^*) = e\left(1 - \frac{5}{2}\frac{a^3}{(a^2+\sigma^{*2})^{\frac{3}{2}}} + \frac{3}{2}\frac{a^5}{(a^2+\sigma^{*2})^{\frac{5}{2}}}\right), \qquad q_0^*(\sigma^*) = 0, \qquad x^* = -\frac{\sigma^{*2}}{16} + \eta_0^*,$$

where $a = \frac{3}{2}(1+0.9e)^{\frac{1}{2}}$ and e is a chosen-parameter modulating the free-surface profile and we respectively set $e = 0.1$, $\alpha = 1/50$ and $l = 20\ m$. We refer the reader to [13] for the whole description of the exact solution. We performed an extensive set of computation with various polynomial degrees and mesh refinement, allowing to assess the global flawless behavior of the algorithm. We highlight these results on Fig. 10 by showing the corresponding free-surface profiles obtained at various discrete times during the evolution up to $T_f \coloneqq 100$, for two particular combinations $k = 3$ / $n_{\text{el}} = 50$ (left) and $k = 8$ / $n_{\text{el}} = 10$ (right). We observe an excellent matching between the numerical solution and the exact values, observing the rise of the shoreline above the mean sea-level before asymptotically settles back to it, without oscillating and breaking. It is remarkable that such a robust behavior is also observed using only 10 large mesh elements and clearly emphasize the subcell resolution capability of this approach: a large part of the shoreline motion occurs in only one cell, while still ensuring a very good agreement with the exact values.

Periodic C&G solution

Simulation parameters.

Computational domain: $\Omega = [-20, 6]$
Number of cells: $n_{\text{el}} = 50, 10$ cells
Boundary conditions: Dirichlet (left) & homogeneous Neumann (right)

Polynomial degree: $k = 3, 8$
Time-marching order: $p = 1$
Final time: $t_{\max} = 300$ sec

The computations associated with the *periodic C&G* solution are more demanding than for the previous test: a monochromatic wave is let run-up and run-down on a plane beach, for an arbitrary large number of time-periods. The computed solution accounts for both shoreward-traveling and reflected waves, generating a periodic

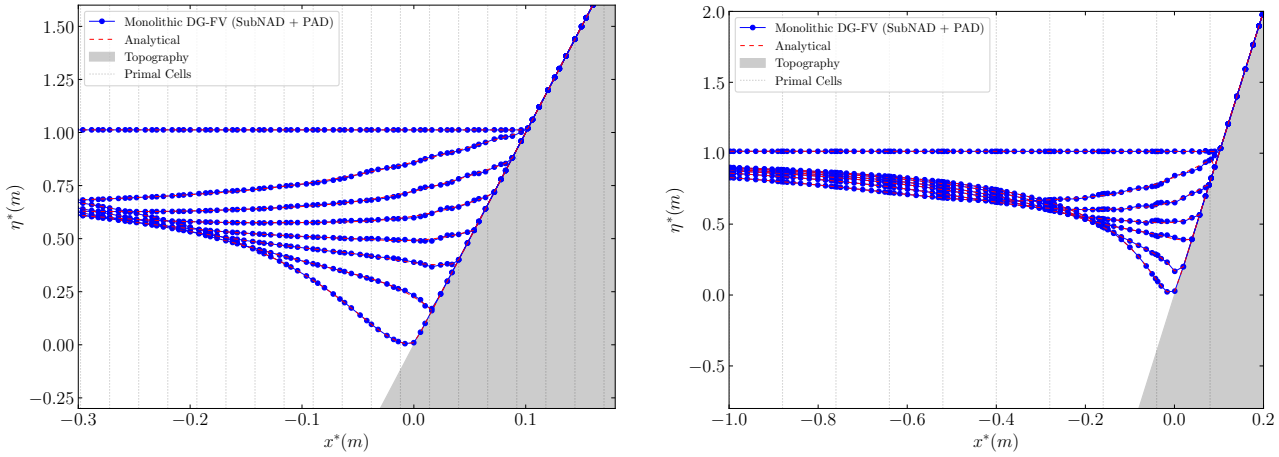

Figure 10: Test 4 - Carrier & Greenspan's transient solution - Free surface elevation computed at several times between 0 and 100 sec: for $k = 3$ and $n_{\text{el}} = 50$ with a zoom on the wet-dry area (left), for $k = 8$ and $n_{\text{el}} = 10$ for the full domain (right).

standing wave on a plane beach involving periodic shoreline oscillations, with an exact description also provided through the hodograph transformation. For the sake of conciseness, we refer again the reader to [13] for a complete description of the corresponding formula, and we consider a solution obtained for a dimensionless amplitude $A^* = 0.6$ and a dimensionless frequency $\omega^* = 1$, corresponding to a non-breaking wave, together with a length scale $l = 20\ m$ and a bottom slope $\alpha = 1/30$, computing the time evolution up to a large number of time-periods. Some snapshots of the free-surface elevation plotted at several discrete times in the range $[20.25T, 20.50T]$, where T refers to the time-period of the periodic motion, are shown in Figs.11 and compared with the exact solution, focusing again on the two particular combinations $k = 3$ / $n_{\text{el}} = 50$ (left) and $k = 8$ / $n_{\text{el}} = 10$ (right). These results confirm the resulting combination of accuracy, robustness and high-resolution associated with the numerical method as there is no noticeable phase-shift even after thousands of computational periods.

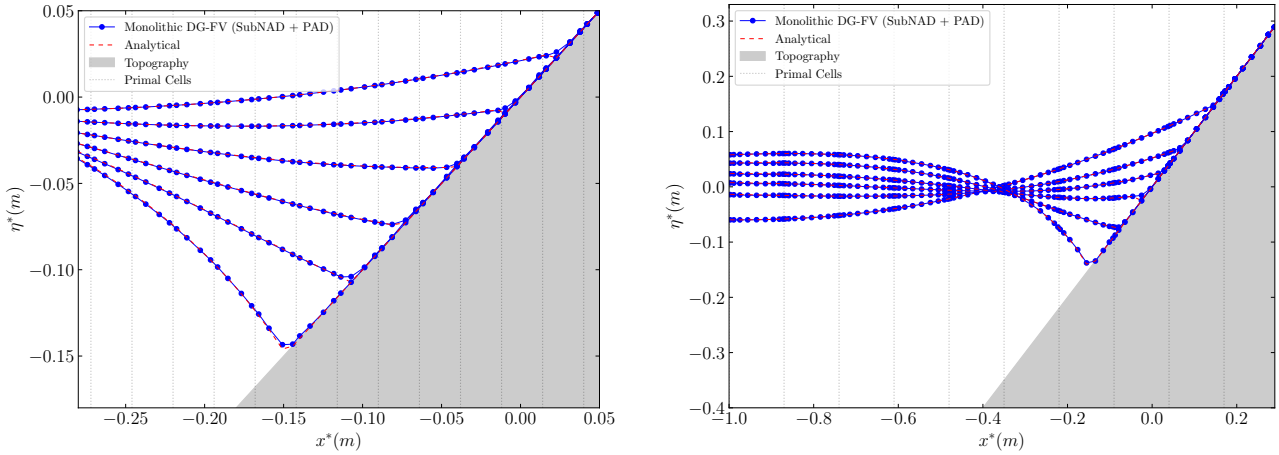

Figure 11: Test 4 - Carrier & Greenspan's periodic solution - Free-surface elevation computed in the time interval $[20.25T, 20.50T]$: for $k = 3$ and $n_{\text{el}} = 50$ with a zoom on the wet-dry interface, and for $k = 8$ and $n_{\text{el}} = 10$ for the full domain (right).

5.5. Periodic oscillations in a parabolic basin

Simulation parameters.

Computational domain: $\Omega = [0, 4]$
Number of cells: $n_{\text{el}} = 50, 30$ cells
Boundary conditions: solid wall

Polynomial degree: $k = 3, 6$
Time-marching order: $p = 3$
Final time: $t_{\max} = 10.0303$ sec

This fifth test-case is dedicated to the study of the oscillations of a planar free-surface in a bowl with a parabolic profile. The corresponding bathymetry is defined as follows:

$$b(x) \coloneqq h_c \left(\frac{1}{a^2} \left(x - \frac{L}{2} \right)^2 - 1 \right),$$

and the initial free-surface is given by

$$h_0(x) \coloneqq \begin{cases} -h_c \left(\left(\frac{1}{a} \left(x - \frac{L}{2} \right) + \frac{B}{\sqrt{2gh_c}} \right)^2 - 1 \right) & \text{for } x_1(0) \leq x \leq x_2(0), \\ 0 & \text{elsewhere,} \end{cases} \qquad q_0(x) \coloneqq 0.$$

with $B = \frac{\sqrt{2gh_0}}{2a}$, $a = 1$, $h_c = 0.5$ and $L = 4$. The corresponding time-evolving solution is periodic with a free-surface that remains planar during evolution, the reader is referred to [20] for the complete formula, in particular for the description of the wet/dry interfaces locations $x_1(t)$ and $x_2(t)$. In the proposed computation, we consider $t_{\max} = 10.0303$ sec (corresponding to 5 periods of fluid oscillations in the bowl). We show on Fig. 12 a comparison between the numerical results and the exact solution after 5 periods, in the time interval $[4T, 5T]$, obtained with $k = 6$ and $n_{\text{el}} = 30$, with an excellent agreement even considering the very coarse discretization. We also compute the global L^2-errors associated with the computation of η, for increasing approximating polynomial's degrees, and increasing mesh levels of refinement, computed at $t = 1$ sec. As expected, the singularities occurring in the solution at the wet/dry interfaces reduces the regularity of the solution and, as a consequence, do not allow to observe the same optimal convergence rates as for the smooth solutions of Test 1. Still, we observe that the method generates stable solutions for all combinations of degree/mesh, and that the accuracy of the scheme increases substantially for higher polynomial degrees (with convergent behaviors and computational orders generally greater than 1).

5.6. Oscillating dam-break

Simulation parameters.

Computational domain: $\Omega = [-210, 210]$
Number of cells: $n_{\text{el}} = 800$ cells
Boundary conditions: solid wall

Polynomial degree: $k = 2$
Time-marching order: $p = 3$
Final time: $t_{\max} = 47,5$ sec

This test-case is devoted to the assessment of the numerical method extension for the GN equations (4)-(5)-(6). Inspired from [50], we investigate the dam-break problem for the GN model, with the following initial data:

$$\eta_0(x) \coloneqq \frac{H_L - H_R}{2} \left(1 - \tanh\left(\frac{x}{\chi} \right) \right), \quad q_0(x) = 0.,$$

and $H_L = 1.8$, $H_R = 1$ and $\chi = 0.4$, which is a regularized piecewise-constant initial data, with a sharp variation initially located at $x = 0$. Note that according to Remark 2.2 concerning the smoothness of the solution for large time evolution, no additional stabilization mechanism is needed and we only apply condition (33) during the computations. We show on Fig.13 the surface profile observed at $t = 47.5\,s$, and we observe that the initial high-gradient area has divided into an oscillating shock-wave propagating rightward, and a rarefaction wave propagating leftward. There is no closed-form for this transient oscillating solution, but as pointed out in [34], the analysis of the Witham system for the GN equations and of Riemann invariants of the NSW equations leads to some approximations of the mean flow values dividing the rarefaction and the dispersive shock areas, and denoted by (H*, u*), see Fig. 13.

$$H^\star = \left(\frac{\sqrt{H_L} + \sqrt{H_R}}{2} \right)^2, \quad u^\star = \left(\sqrt{gH^\star} - \sqrt{gH_R} \right).$$

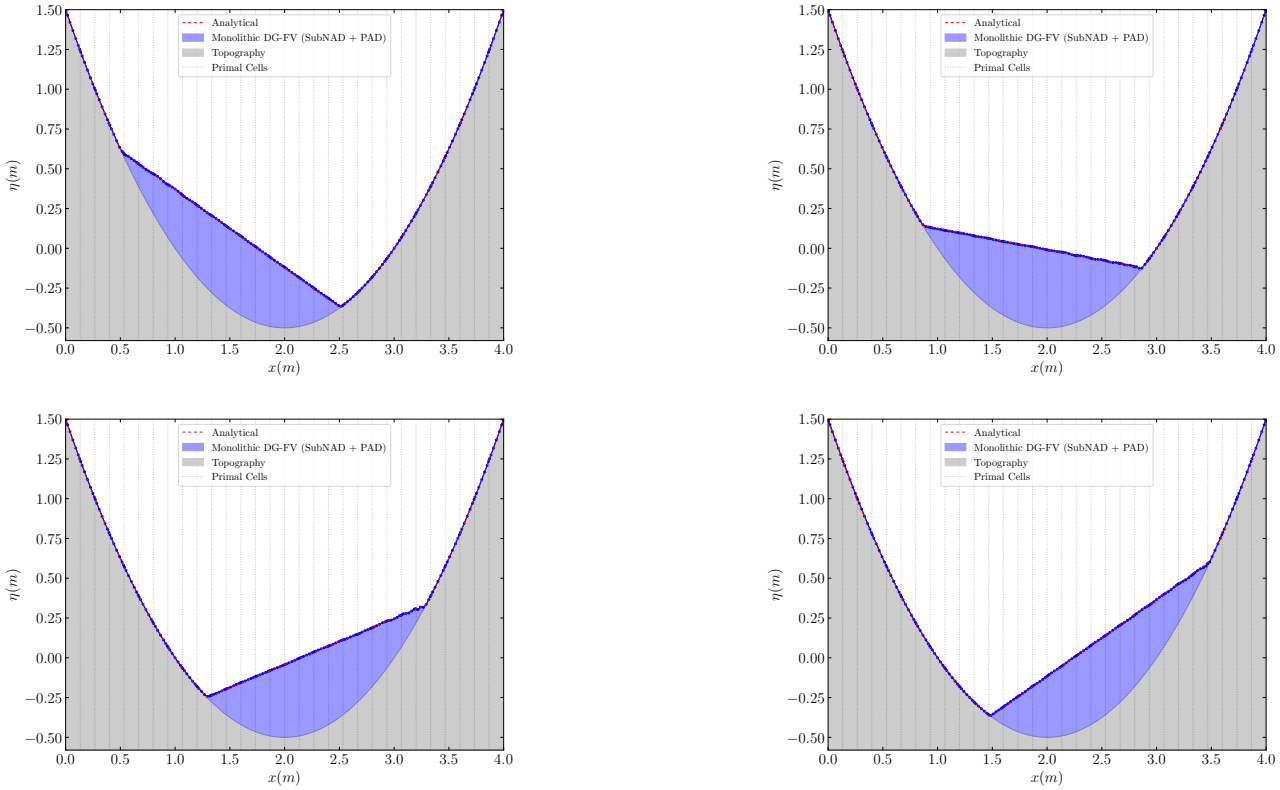

Figure 12: Test 5 - Periodic planar surface in a parabolic basin - Snapshots of the free-surface elevation, computed in the time interval $[4, 4.5T]$ for $k = 6$ and $n_{\text{el}} = 30$.

We observe that these approximate values are correctly estimated by the model. Note also that an approximation of the leading soliton's amplitude is available, denoted by a^+, also accurately reproduced, see again Fig.13 and we observe a very good resolution of the highly oscillatory behavior, with a regular modulating envelope's profile corresponding to those usually observed with very much finer meshes.

5.7. Solitary-waves over a piecewise-linear bottom

Simulation parameters.

Computational domain: $\Omega = [-24, 12]$
Number of cells: $n_{\text{el}} = 150$ cells
Boundary conditions: solid wall

Polynomial degree: $k = 2$
Time-marching order: $p = 3$
Final time: $t_{\max} = 7,5$ sec

In this last test-case, we consider the propagation of a solitary-wave, which is a surface perturbation propagating without any temporal evolution in shape or size when viewed in the reference frame moving with the group velocity of the wave. The GN equations (4) do have solitary-wave solutions defined as follows:

$$\begin{cases} \eta(t,x) = H_0 + \epsilon H_0 \text{sech}^2\left(\kappa(x - ct)\right), \\ q(t,x) = c\left(\eta(t,x) - H_0\right), \end{cases} \tag{45}$$

where ϵ is the amplitude of the wave and $\kappa := \sqrt{\dfrac{3\epsilon}{4H_0^2(1+\epsilon)}}$ and $c := \sqrt{gH_0(1+\epsilon)}$. For this particular test-case, the computational domain is a $36\,m$ channel with a flat bottom for $x \leq 0$ followed by a linear profile with a slope $1:30$, and a solitary wave propagates from the left boundary, with a water level at rest $H_0 = 0.25\,m$. Measurements of the free-surface are available at various locations along the channel, obtained from wave-gauges from the laboratory study performed at LEGI (Grenoble, France, see [39]). We consider 4 series of experiments, involving increasing waves amplitudes, from $\epsilon = 0.096$ to $\epsilon = 0.534$, which stand for highly nonlinear evolutions. For each experiment, we compare the numerical results with time-series of the free-surface elevation at wave gauges locations (we do not recall the exact location of the gauges, which may be found, for instance, in Table

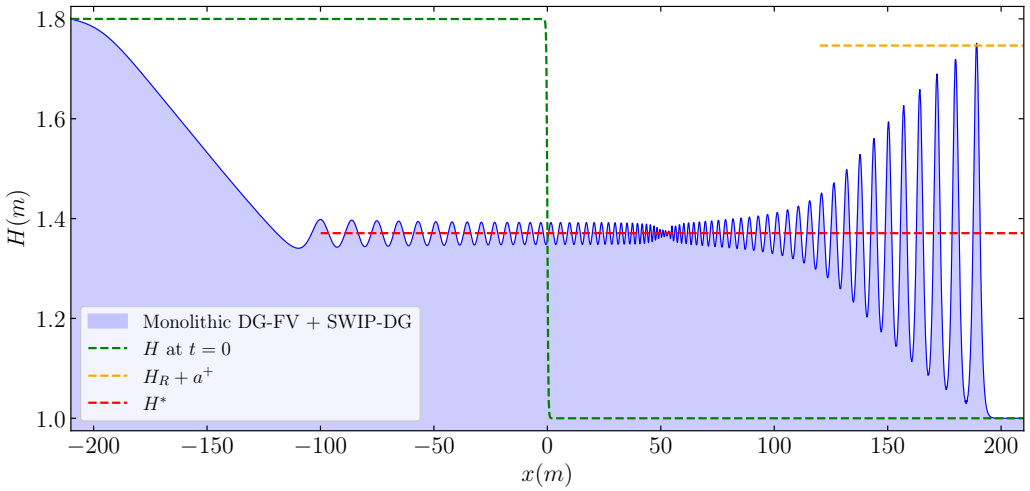

Figure 13: Test 6 - Oscillating dam-break - Free-surface elevation computed for $k = 2$ and $n_{\text{el}} = 800$ at time $t = 47,5\,s$. Comparison with mean values obtained from Witham-like analysis.

2 of [11]). As displayed in Fig. 14, we observe some excellent agreements, especially regarding the maximum surface elevation during the shoaling process, and considering the low number of mesh elements. The wave asymetrical profile is also accurately reproduced even in the most nonlinear cases. We emphasize that neither stabilization process is needed, nor additional filtering treatment to control possible aliasing effects due to the numerical approximations of highly nonlinear processes.

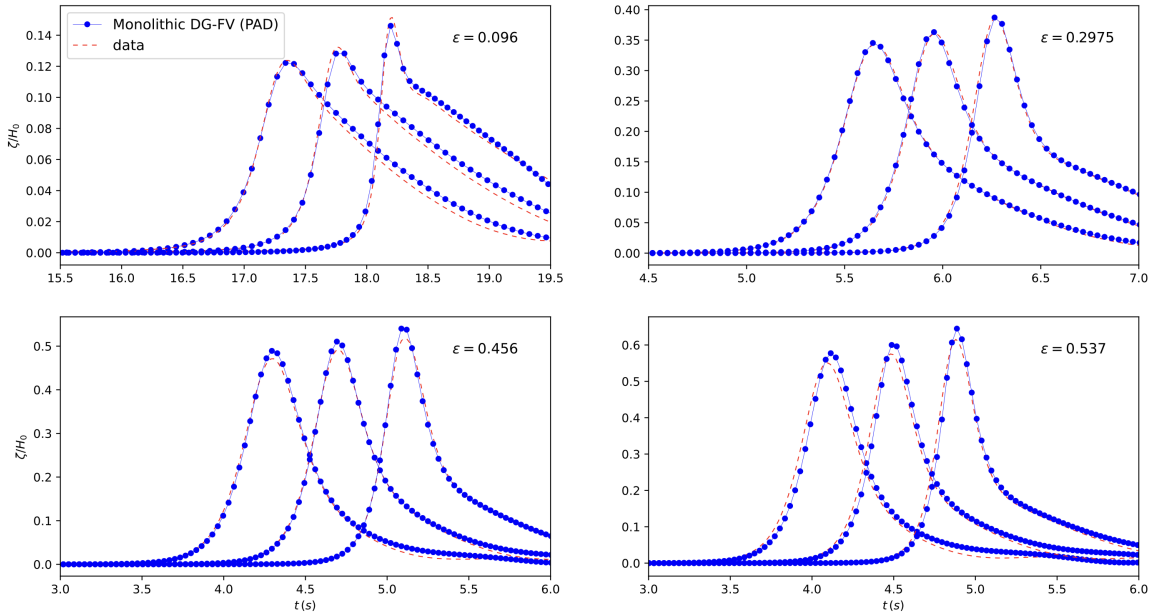

Figure 14: Test 7 - Solitary-waves shoaling over a piecewise-linear bottom - Time-series of free-surface elevation at 3 locations along the channel, for 4 different wave amplitudes.

6. Conclusion

In this paper, we introduce a high-order *local subcell monolithic DG/FV* discretization method for the approximation of nonlinear free-surface shallow-water equations with different source terms. We also detail an original combination of local subcell monolithic DG/FV and IP-DG methods, in order to approximate the higher-order GN equations. Several test-cases have been studied and they confirm that this new strategy is promising both to suppress spurious oscillations near flow discontinuities and to ensure the robustness in the vicinity of wet-dry fronts, even with a very low-mesh resolution but some large enough degrees of polynomial approximation.

Subsequent works may concern the extension to the two-dimensional horizontal surface model, as well as the coupling with wave generation and floating structures models. This strategy also open the door for the design of more refined admissibility filtering for the numerical study of some singularities of particular types, which are sometimes observed in the process of wave-breaking, like peaked-waves.

Acknowledgements

F.M. was partly supported by the Service Hydrographique et Océanographique de la Marine (SHOM) and by the French National Research Agency project BOURGEONS, grant ANR-23-CE40-0014.

Appendix A - Water-height positivity for intermediate Riemann states.

Using Forward-Euler time integration with the CFL condition (11), we can write the formulation (16) with subcell FV fluxes (uniformly setting the blending coefficients $\Theta_{i+\frac{1}{2}} = 0$, as

$$\overline{\mathbf{v}}_m^{n+1} = \overline{\mathbf{v}}_m^n - \frac{\Delta t^n}{|S_m|}\left(\boldsymbol{\mathcal{F}}^{\mathrm{FV},-}_{m+\frac{1}{2}} - \boldsymbol{\mathcal{F}}^{\mathrm{FV},+}_{m-\frac{1}{2}}\right) + \Delta t^n \overline{\mathbf{S}}_m^n, \tag{46}$$

where we dropped the superscript i.

Proposition 6.1. *The lowest-order FV fluxes on subcells* (46) *ensures the water-height positivity for the associated Riemann intermediate states.*

Proof. We add and subtract the required quantities in order to make appearing a suitable convex combination of intermediate solution states:

$$\begin{aligned}
\overline{\mathbf{v}}_m^{n+1} &= \overline{\mathbf{v}}_m^n - \frac{\Delta t^n}{|S_m|}\left(\boldsymbol{\mathcal{F}}^{\mathrm{FV},-}_{m+\frac{1}{2}} - \boldsymbol{\mathcal{F}}^{\mathrm{FV},+}_{m-\frac{1}{2}}\right) + \Delta t^n \overline{\mathbf{S}}_m^n \pm \frac{2\Delta t^n}{|S_m|}\sigma\overline{\mathbf{v}}_m^n \pm \frac{\Delta t^n}{|S_m|}\mathbf{F}(\overline{\mathbf{v}}_m^n) \\
&= \left(1 - \frac{2\Delta t^n}{|S_m|}\sigma\right)\overline{\mathbf{v}}_m^n + \frac{\Delta t^n}{|S_m|}\sigma\left(\overline{\mathbf{v}}_m^n - \frac{\boldsymbol{\mathcal{F}}^{\mathrm{FV},-}_{m+\frac{1}{2}} - \mathbf{F}(\overline{\mathbf{v}}_m^n)}{\sigma}\right) + \frac{\Delta t^n}{|S_m|}\sigma\left(\overline{\mathbf{v}}_m^n + \frac{\boldsymbol{\mathcal{F}}^{\mathrm{FV},+}_{m-\frac{1}{2}} - \mathbf{F}(\overline{\mathbf{v}}_m^n)}{\sigma}\right) + \Delta t^n \overline{\mathbf{S}}_m^n \\
&= \left(1 - \frac{2\Delta t^n}{|S_m|}\sigma\right)\overline{\mathbf{v}}_m^n + \frac{\sigma\Delta t^n}{|S_m|}\mathbf{v}^{*,-}_{m+\frac{1}{2}} + \frac{\sigma\Delta t^n}{|S_m|}\mathbf{v}^{*,+}_{m-\frac{1}{2}} + \Delta t^n \overline{\mathbf{S}}_m^n,
\end{aligned}$$

where

$$\mathbf{v}^{*,-}_{m+\frac{1}{2}} := \overline{\mathbf{v}}_m^n - \frac{\boldsymbol{\mathcal{F}}^{\mathrm{FV},-}_{m+\frac{1}{2}} - \mathbf{F}(\overline{\mathbf{v}}_m^n)}{\sigma}, \qquad \mathbf{v}^{*,+}_{m-\frac{1}{2}} := \overline{\mathbf{v}}_m^n + \frac{\boldsymbol{\mathcal{F}}^{\mathrm{FV},+}_{m-\frac{1}{2}} - \mathbf{F}(\overline{\mathbf{v}}_m^n)}{\sigma}.$$

It is enough to ensure that for all $m \in [\![1, k+1]\!]$, $\overline{\eta}_m^n \geq \overline{b}_m$. Dropping also the superscript n, we observe that this may be achieved for any $m \in [\![1, k+1]\!]$ if

$$\eta^{*,-}_{m+\frac{1}{2}} := \overline{\eta}_m - \frac{\boldsymbol{\mathcal{F}}^{\mathrm{FV},(1),-}_{m+\frac{1}{2}} - \overline{q}_m}{\sigma} \geq \overline{b}_m, \quad \text{and} \quad \eta^{*,+}_{m-\frac{1}{2}} := \overline{\eta}_m + \frac{\boldsymbol{\mathcal{F}}^{\mathrm{FV},(1),+}_{m-\frac{1}{2}} - \overline{q}_m}{\sigma} \geq \overline{b}_m,$$

where the fluxes are

$$\boldsymbol{\mathcal{F}}^{\mathrm{FV},(1),-}_{m+\frac{1}{2}} = \frac{\overline{q}_m^+ + \overline{q}_{m+1}^-}{2} - \frac{\sigma}{2}\left(\overline{\eta}_{m+1}^- - \overline{\eta}_m^+\right), \qquad \boldsymbol{\mathcal{F}}^{\mathrm{FV},(1),+}_{m-\frac{1}{2}} = \frac{\overline{q}_{m-1}^+ + \overline{q}_m^-}{2} - \frac{\sigma}{2}\left(\overline{\eta}_m^- - \overline{\eta}_{m-1}^+\right).$$

Noticing that $\overline{\eta}_{m+1}^- - \overline{\eta}_m^+ = \overline{H}_{m+1}^- - \overline{H}_m^+ + \overline{b}_{m+1}^- - \overline{b}_m^+ = \overline{H}_{m+1}^- - \overline{H}_m^+$, and working with velocity $\overline{u}_m := \frac{\overline{q}_m}{\overline{H}_m}$, we can write

$$\begin{aligned}
\eta^{*,-}_{m+\frac{1}{2}} &= \overline{\eta}_m - \frac{\boldsymbol{\mathcal{F}}^{\mathrm{FV},(1),-}_{m+\frac{1}{2}} - \overline{q}_m}{\sigma} = \overline{H}_m + \overline{b}_m - \frac{\boldsymbol{\mathcal{F}}^{\mathrm{FV},(1),-}_{m+\frac{1}{2}} - \overline{q}_m}{\sigma}, \\
&= \frac{1}{2}\left(2\overline{H}_m - \overline{H}_m^+ + \overline{H}_{m+1}^-\right) - \frac{1}{2\sigma}\left(\overline{H}_{m+1}^-\overline{u}_m + \overline{H}_m^+\overline{u}_m - 2\overline{H}_m\overline{u}_m\right) + \overline{b}_m.
\end{aligned}$$

This way, it is enough to ensure that

$$\frac{1}{2}\left(2\overline{H}_m - \overline{H}_m^+ + \overline{H}_{m+1}^-\right) - \frac{1}{2\sigma}\left(\overline{H}_{m+1}^-\overline{u}_m + \overline{H}_m^+\overline{u}_m - 2\overline{H}_m\overline{u}_m\right) \geq 0.$$

By construction, for any $p \in [\![1, k+1]\!]$, $0 \leq \overline{H}_p^{\pm} \leq \overline{H}_p$, so we have easily $2\overline{H}_m - \overline{H}_m^+ + \overline{H}_{m+1}^- \geq 2\overline{H}_m$. For the other term, let us reformulate it as

$$\overline{H}_{m+1}^- \overline{u}_m + \overline{H}_m^+ \overline{u}_m - 2\overline{H}_m \overline{u}_m = \left(2\overline{H}_m - \overline{H}_m^+\right) \frac{1 + \overline{u}_m \sigma^{-1}}{2} + \overline{H}_{m+1}^- \frac{1 - \overline{u}_{m+1}\sigma^{-1}}{2},$$

and according to CFL (11), we easily have:

$$2\overline{H}_m - \overline{H}_m^+ \geq \overline{H}_m, \qquad \frac{1 + \overline{u}_m \sigma^{-1}}{2} \geq 0, \qquad \overline{H}_{m+1}^- \geq 0, \qquad \frac{1 - \overline{u}_{m+1}\sigma^{-1}}{2} \geq 0.$$

Gathering all the results ensures that $\eta_{m+\frac{1}{2}}^{*,-} \geq \overline{b}_m$ and a similar result may be achieved for $\eta_{m-\frac{1}{2}}^{*,+} \geq \overline{b}_m$. □

Appendix B - Blending coefficients for the subNAD criterion.

Let us define the admissible envelope associated with a finite family $(a_i)_{i \in [\![1,k]\!]} \in \mathbb{R}^k$ as

$$\mathcal{J}(a_1, \ldots, a_k) := \left[\min_{1 \leq i \leq k} a_i, \max_{1 \leq i \leq k} a_i \right].$$

The fully discrete formulation (18) supplemented with the topography source term $\overline{\mathbf{S}}_m^n := \left(\overline{\mathbf{S}}_m^{n,(1)}, \overline{\mathbf{S}}_m^{n,(2)}\right) = \left(0, \overline{\mathbf{S}}_m^{n,(2)}\right)$ reads as follows:

$$\begin{cases} \overline{\eta}_m^{n+1} = \left(1 - \dfrac{2\Delta t^n}{|S_m|}\sigma\right) \overline{\eta}_m^n + \dfrac{\sigma \Delta t^n}{|S_m|} \widetilde{\eta}_{m+\frac{1}{2}}^{*,-} + \dfrac{\sigma \Delta t^n}{|S_m|} \widetilde{\eta}_{m+\frac{1}{2}}^{*,+}, \\ \overline{q}_m^{n+1} = \left(1 - \dfrac{2\Delta t^n}{|S_m|}\sigma\right) \overline{q}_m^n + \dfrac{\sigma \Delta t^n}{|S_m|} \widetilde{q}_{m+\frac{1}{2}}^{*,-} + \dfrac{\sigma \Delta t^n}{|S_m|} \widetilde{q}_{m+\frac{1}{2}}^{*,+} + \Delta t^n \overline{\mathbf{S}}_m^{n,(2)}. \end{cases}$$

Focusing on the first equation, the two blended intermediate states (19) read as:

$$\widetilde{\eta}_{m+\frac{1}{2}}^{*,\pm} = \eta_{m+\frac{1}{2}}^{*,\pm} \pm \Theta_{m+\frac{1}{2}} \left(\frac{\widehat{\mathbf{F}}_{m+\frac{1}{2}}^{(1)} - \boldsymbol{\mathcal{F}}_{m+\frac{1}{2}}^{(1),-}}{\sigma} \right).$$

Now respectively denoting by

$$[\alpha_m, \beta_m] := \mathcal{J}\left(\overline{\eta}_{m-1}, \overline{\eta}_m, \overline{\eta}_{m+1}, \eta_{m-\frac{1}{2}}^{*,+}, \eta_{m+\frac{1}{2}}^{*,-}\right), \qquad [\alpha_{m+1}, \beta_{m+1}] := \mathcal{J}\left(\overline{\eta}_m, \overline{\eta}_{m+1}, \overline{\eta}_{m+2}, \eta_{m+\frac{1}{2}}^{*,+}, \eta_{m+\frac{3}{2}}^{*,-}\right)$$

the local admissible envelopes associated with the subcells m and $m+1$, the pevious Appendix A ensures that we have

$$\left(\eta_{m+\frac{1}{2}}^{*,-}, \eta_{m+\frac{1}{2}}^{*,+}\right) \in [\alpha_m, \beta_m] \times [\alpha_{m+1}, \beta_{m+1}],$$

si that we aim at ensuring that the blended intermediate states also satisfy

$$\left(\widetilde{\eta}_{m+\frac{1}{2}}^{*,-}, \widetilde{\eta}_{m+\frac{1}{2}}^{*,+}\right) \in [\alpha_m, \beta_m] \times [\alpha_{m+1}, \beta_{m+1}].$$

This may be obtained with the following choice:

$$\Theta_{m+\frac{1}{2}} \leq \min \left(1, \left| \frac{\sigma}{\Delta \mathbf{F}_{m+\frac{1}{2}}^{(1),-}} \right| \begin{cases} \min\left(\beta_{m+1} - \eta_{m+\frac{1}{2}}^{*,+},\ \eta_{m+\frac{1}{2}}^{*,-} - \alpha_m\right) & \text{if } \Delta \mathbf{F}_{m+\frac{1}{2}}^{(1),-} > 0, \\ \min\left(\beta_m - \eta_{m+\frac{1}{2}}^{*,-},\ \eta_{m+\frac{1}{2}}^{*,+} - \alpha_{m+1}\right) & \text{if } \Delta \mathbf{F}_{m+\frac{1}{2}}^{(1),-} < 0. \end{cases} \right).$$

Appendix C - SWIP-DG discrete bilinear form for the GN elliptic operator

It is shown in [86] that the following identity holds for all smooth enough scalar-valued functions w:

$$\mathscr{L}[H, b]w = \partial_x(-\kappa(H)\partial_x w) - \beta(H, \partial_x b)\partial_x w + \partial_x(\beta(H, \partial_x b)w) + \delta(H, \partial_x b)w, \tag{47}$$

with the coefficient functions defined as follows:

$$\kappa(H) := \frac{1}{3}H^3, \quad \beta(H, \partial_x b) := \frac{\sqrt{3}}{2}\kappa[H]^{\frac{1}{2}}H^{\frac{1}{2}}\partial_x b, \quad \delta(H, \partial_x b) := (H^{\frac{1}{2}}\partial_x b)^2 + H.$$

For any given mesh element ω_i, let us set $\kappa_i := \kappa_{|\omega_i}$, $\beta_i := \beta|_{|\omega_i}$ and $\delta_i := \delta|_{|\omega_i}$. In the following, with use general multi-dimensional notations borrowed from [86], but it is easy to identify that any mesh interface F belonging to the set of mesh interfaces $\mathscr{F}_h$ identifies with a particular mesh nodes $x_{i+\frac{1}{2}}$. We define the jump and weighted average operators such that, for a sufficiently regular function φ and an interior interface $F \in \mathscr{F}_h^i$ shared by two distinct mesh elements ω_1 and ω_2, *i.e.*, $F \subset \partial\omega_1 \cap \partial\omega_2$, we have:

$$[\![\varphi]\!] := \varphi_{|\omega_1} - \varphi_{|\omega_2}, \quad \{\!\{\varphi\}\!\}_{\lambda,F} := \lambda_2\varphi_{|\omega_1} + \lambda_1\varphi_{|\omega_2}, \quad \lambda_i := \frac{\kappa_{\omega_i}}{\kappa_{\omega_1} + \kappa_{\omega_2}}, \quad \forall i \in \{1, 2\}.$$

In the following, and when no confusion arises, we omit the subscript F from both $[\![\varphi]\!]$ and $\{\!\{\varphi\}\!\}$. The definition of the average and jump operators at boundary vertices depends on the selected variable, according to the prescribed boundary conditions. The definition of the proposed discrete bilinear form $\mathscr{L}_h(\kappa, \beta, \delta; \cdot, \cdot)$ on $\mathbb{P}^k(\mathscr{T}_h) \times \mathbb{P}^k(\mathscr{T}_h)$ is:

$$\begin{aligned}\mathscr{L}_h(\kappa, \beta, \delta; v_h, w_h) := &\sum_{\omega\in\mathscr{T}_h}\int_\omega \kappa\partial_x v_h\partial_x w_h \,\mathrm{d}x - \sum_{\omega\in\mathscr{T}_h}\int_\omega \beta v_h\partial_x w_h \,\mathrm{d}x - \sum_{\omega\in\mathscr{T}_h}\int_\omega \partial_x v_h\beta w_h \,\mathrm{d}x + \sum_{\omega\in\mathscr{T}_h}\int_\omega \delta v_h w_h \,\mathrm{d}x \\ &+ \sum_{F\in\mathscr{F}_h}\gamma_{\kappa,F}[\![v_h]\!][\![w_h]\!] - \sum_{F\in\mathscr{F}_h}\left(\{\!\{\kappa\partial_x v_h\}\!\}_\lambda[\![w_h]\!] + [\![v_h]\!]\{\!\{\kappa\partial_x w_h\}\!\}_\lambda\right) + \sum_{F\in\mathscr{F}_h}\left(\{\!\{\beta v_h\}\!\}_\lambda[\![w_h]\!] + [\![v_h]\!]\{\!\{\beta w_h\}\!\}_\lambda\right).\end{aligned}$$

The κ-dependent penalty parameter $\gamma_{\kappa,F}$ is defined as follows:

$$\gamma_{\kappa,F} := \begin{cases}\xi_F\frac{2\kappa_{\omega_1}\kappa_{\omega_2}}{\kappa_{\omega_1}+\kappa_{\omega_2}}, & \text{if } F \in \mathscr{F}_h^i \text{ such that } F = \partial\omega_1 \cap \partial\omega_2, \\ \xi_F\kappa_\omega, & \text{if } F \in \mathscr{F}_h^b \text{ such that } F = \partial\omega \cap \partial\Omega.\end{cases} \tag{48}$$

In (48), ξ_F denotes a user-defined parameter sufficiently large to ensure coercivity. We refer the reader to [86] for a complete description.

References

[1] F. Alcrudo and P. Garcia-Navarro. A high-resolution godunov-type scheme in finite volumes for the 2d shallow-water equations. *Internat. J. Numer. Methods Fluids*, 1993.

[2] K. Anastasiou and C. Chan. Solution of the 2d shallow water equations using the finite volume method on unstructured triangular meshes. *Int J Numer Methods Fluids*, 24:1225–1245, 1997.

[3] L. Arpia and M. Ricchiuto. Well balanced residual distribution for the ALE spherical shallow water equations on moving adaptive meshes. *J. Comput. Phys.*, 405:109–173, 2019.

[4] E. Audusse, F. Bouchut, M.-O. Bristeau, R. Klein, and B. Perthame. A fast and stable well-balanced scheme with hydrostatic reconstruction for shallow water flows. *SIAM J. Sci. Comput.*, 25(6):2050–2065, 2004.

[5] D. Balsara, C. Altmann, C. Munz, and M. Dumbser. A sub-cell based indicator for troubled zones in RKDG schemes and a novel class of hybrid RKDG+HWENO schemes. *J. Comp. Phys.*, 226:586–620, 2007.

[6] S. Barros and J. Cardenas. A nonlinear galerkin method for the shallow-water equations on periodic domains. *J. Comput. Phys.*, 172:592–608, 2001.

[7] A. Bermudez, A. Dervieux, J.-A. Desideri, and M. Vazquez. Upwind schemes for the two-dimensional shallow water equations with variable depth using unstructured meshes. *Comput. Methods Appl. Mech. Engrg.*, 155:49–72, 1998.

[8] C. Berthon and F. Marche. A positive preserving high order VFRoe scheme for shallow water equations: a class of relaxation schemes. *SIAM J. Sci. Comput.*, 30(5):2587–2612, 2008.

[9] C. Berthon, F. Marche, and R. Turpault. An efficient scheme on wet/dry transitions for shallow water equations with friction. *Comput. Fluids*, 48(1):192 – 201, 2011.

[10] R. Biswas, K. D. Devine, and J. E. Flaherty. Parallel, adaptive finite element methods for conservation laws. *Applied Numerical Mathematics*, 14:255 – 283, 1994.

[11] P. Bonneton, F. Chazel, D. Lannes, F. Marche, and M. Tissier. A splitting approach for the fully nonlinear and weakly dispersive Green-Naghdi model. *J. Comput. Phys.*, 230(4):1479 – 1498, 2011.

[12] A. Canestrelli, A. Siviglia, M. Dumbser, and E. Toro. Well-balanced high-order centred schemes for non-conservative hyperbolic systems. applications to shallow water equations with fixed and mobile bed. *Advances in Water Resources*, 32(6):634–644, 2009.

[13] G. Carrier and H. Greenspan. Water waves of finite amplitude on a sloping beach. *Journal of Fluid Mechanics*, 2:97—109, 1958.

[14] E. Casoni, J. Peraire, and A. Huerta. One-dimensional shock-capturing for high-order discontinuous Galerkin methods. *Int. J. Numer. Meth. Fluids*, 71:737–755, 2013.

[15] M. Castro Diaz, J. Lopez-Garcia, and C. Parès. High order exactly well-balanced numerical methods for shallow water systems. *J. Comput. Phys.*, 246:242–264, 2013.

[16] F. Chazel, D. Lannes, and F. Marche. Numerical simulation of strongly nonlinear and dispersive waves using a Green-Naghdi model. *J. Sci. Comput.*, 48:105–116, 2011.

[17] S. Clain, S. Diot, and R. Loubère. A high-order finite volume method for systems of conservation laws—multi-dimensional optimal order detection (mood). *J. Comput. Phys.*, 230:4028–4050, 2011.

[18] B. Cockburn, S. Hou, and C.-W. Shu. The Runge-Kutta Discontinuous Galerkin Method for Conservation Laws V: Multidimensional Systems. *J. Comp. Phys.*, 141:199–224, 1998.

[19] J. N. de la Rosa and C. D. Munz. Hybrid DG/FV schemes for magnetohydrodynamics and relativistic hydrodynamics. *Comp. Phys. Commun.*, 222:113–135, 2018.

[20] O. Delestre, C. Lucas, P.-A. Ksinant, F. Darboux, C. Laguerre, T.-N. Tuoi Vo, F. James, and S. Cordier. SWASHES: a compilation of shallow water analytic solutions for hydraulic and environmental studies. *Internat. J. Numer. Methods Fluids*, 72(3):269–300, 2012.

[21] D. A. Di Pietro and A. Ern. *Mathematical Aspects of Discontinuous Galerkin Methods*, volume 69 of *Mathématiques and Applications*. Springer, 2012.

[22] D. A. Di Pietro and F. Marche. Weighted interior penalty discretization of fully nonlinear and weakly dispersive free surface shallow water flows. *J. Comput. Phys.*, 355:285–309, 2018.

[23] S. Diot, S. Clain, and R. Loubère. Improved detection criteria for the multi-dimensional optimal order detection (MOOD) on unstructured meshes with very high-order polynomials. *Computers and Fluids*, 64:43–63, 2012.

[24] S. Diot, R. Loubère, and S. Clain. The MOOD method in the three-dimensional case: very-high-order finite volume method for hyperbolic systems. *Int. J. Numer. Meth. Fluids*, 73:362–392, 2013.

[25] D.Kuzmin. Slope limiting for discontinuous galerkin approximations with a possibly non-orthogonal taylor basis. *Int J Numer Methods Fluids*, 71(9):1178–1190, 2013.

[26] M. Dumbser and R. Loubère. A simple robust and accurate a posteriorisub-cell finite volume limiter for the discontinuousGalerkin method on unstructured meshes. *J. Comp. Phys.*, 319:163–199, 2016.

[27] A. Duran. *Thèse de Doctorat*. Université de Montpellier, 2014.

[28] A. Duran, Q. Liang, and F. Marche. On the well-balanced numerical discretization of shallow water equations on unstructured meshes. *J. Comput. Phys.*, 235:565–586, 2013.

[29] A. Duran and F. Marche. Recent advances on the discontinuous Galerkin method for shallow water equations with topography source terms. *Comput. Fluids*, 101:88–104, 2014.

[30] K. Erduran, V. Kutija, and C. Hewett. Performance of finite volume solutions to the shallow water equations with shock-capturing schemes. *Int J Numer Methods Fluids*, 40:1237–1273, 2002.

[31] L. Fraccarollo and E. Toro. Experimental and numerical assessment of the shallow water model for two-dimensional dam-break type problems. *J. Hydraulic Res.*, 33(6):843–863, 1995.

[32] E. Gaburro, W. Boscheri, S. Chiocchetti, and M. Ricchiuto. Discontinuous galerkin schemes for hyperbolic systems in non-conservative variables: Quasi-conservative formulation with subcell finite volume corrections. *Computer Methods in Applied Mechanics and Engineering*, 431:117311, 2024.

[33] J. Gallardo, C. Parés, and M. Castro. On a well-balanced high-order finite volume scheme for shallow water equations with topography and dry areas. *J. Comput. Phys.*, 227(1):574–601, 2007.

[34] S. Gavrilyuk, B. Nkonga, K.-M. Shyue, and L. Truskinovsky. Generalized Riemann problem for dispersive equations. *preprint - HAL Id : hal-01958328*, 2019.

[35] S. Gottlieb, C.-W. Shu, and T. E. Strong stability preserving high order time discretization methods. *SIAM Review*, 43:89–112, 2001.

[36] A. E. Green and P. M. Naghdi. A derivation of equations for wave propagation in water of variable depth. *Journal of Fluid Mechanics Digital Archive*, 78(02):237–246, 1976.

[37] J.-L. Guermond, R. Pasquetti, and B. Popov. Entropy viscosity method for nonlinear conservation laws. *J. Comput. Phys.*, 230:4248–4267, 2011.

[38] M. Guerra, R. Cienfuegos, C. Escauriaza, F. Marche, and J. Galaz. Modeling rapid flood propagation over natural terrains using a well-balanced scheme. *J. Hydraulic Res.*, 140(7), 2014.

[39] S. Guibourg. *Modélisation numérique et expérimentale des houles bidimensionnelles en zone cotière,*. PhD Thesis, Université Joseph Fourier-Grenoble I, 1994.

[40] A. Haidar, F. Marche, and F. Vilar. A posteriori finite-volume local subcell correction of high-order discontinuous Galerkin schemes for the nonlinear shallow-water equations. *J. Comput. Phys.*, 452:110902, 2022.

[41] A. Haidar, F. Marche, and F. Vilar. Free-boundary problems for wave-structure interactions in shallow-water: Dg-ale description and local subcell correction. *J. Sci. Comput.*, 98(45), 2024.

[42] M. Ioriatti and M. Dumbser. A posteriori sub-cell finite volume limiting of staggered semi-implicit discontinuous Galerkin schemes for the shallow water equations. *Applied Numerical Mathematics*, 135:443–480, 2019.

[43] M. Iskandarani, D. B. Haidvogel, and J. P. Boyd. A staggered spectral element model with application to the oceanic shallow water equations. *Int J Numer Methods Fluids*, 20(5):393–414, 1995.

[44] S. Israwi. Large time existence for 1D Green-Naghdi equations. *Nonlinear Analysis*, 74(81-93), 2011.

[45] T. Kato. The Cauchy problem for quasi-linear symmetric hyperbolic systems. *Arch. Ration. Mech. Anal.*, 58(3):181–205, 1975.

[46] G. Kesserwani and Q. Liang. Well-balanced RKDG2 solutions to the shallow water equations over irregular domains with wetting and drying. *Comput. Fluids*, 39(10):2040–2050, 2010.

[47] R. Kirby and S. Sherwin. Stabilisation of spectral / hp element methods through spectral vanishing viscosity: Application to fluid mechanics. *Comput. Methods Appl. Mech. Engrg.*, 195:3128–3144, 2006.

[48] L. Krivodonova. Limiters for high-order discontinuous Galerkin methods. *J. Comp. Phys.*, 226:879–896, 2007.

[49] D. Kuzmin and M. de Luna. Subcell flux limiting for high-order bernstein finite element discretizations of scalar hyperbolic conservation laws. *J. Comp. Phys.*, 411:109411, 2020.

[50] O. Le Métayer, S. Gavrilyuk, and S. Hank. A numerical scheme for the Green-Naghdi model. *J. Comput. Phys.*, 34(229):2034–2045, 2010.

[51] S. Le Roy, R. Pedreros, C. André, F. Paris, S. Lecacheux, F. Marche, and C. Vinchon. Coastal flooding of urban areas by overtopping: dynamic modelling application to the Johanna storm (2008) in Gavres (France). *Nat. Hazards Earth Syst. Sci.*, 15:2497–2510, 2014.

[52] P. Lesaint and P.-A. Raviart. On a finite element method to solve the neutron transport equation. In C. de Boor, editor, *Partial Differential Equations*. Academic Press, New York, 1974.

[53] L. Li and Q. Zhang. A new vertex-based imiting approach for nodal discontinuous galerkin methods on arbitrary unstructured meshes. *Comput. Fluids*, 159:316–326, 2017.

[54] Q. Liang and F. Marche. Numerical resolution of well-balanced shallow water equations with complex source terms. *Advances in Water Resources*, 32(6):873 – 884, 2009.

[55] Y. Lin and J. Chan. High order entropy stable discontinuous galerkin spectral element methods through subcell limiting. *J. Comp. Phys.*, 498:112677, 2024.

[56] H. Ma. A spectral element basin model for the shallow water equations. *J. Comput. Phys.*, 109(1):133 – 149, 1993.

[57] F. Marche. Combined Hybridizable Discontinuous Galerkin (HDG) and Runge-Kutta Discontinuous Galerkin (RK-DG) formulations for Green-Naghdi equations on unstructured meshes. *J. Comput. Phys.*, 418:109637, 2020.

[58] A. Meister and S. Ortleb. A positivity preserving and well-balanced DG scheme using finite volume subcells in almost dry regions. *Appl. Math. Comp.*, 272:259–273, 2016.

[59] V. Michel-Dansac. A well-balanced scheme for the shallow-water equations with topography. *Computers and Mathematics with Applications*, 72(3):568–593, 2016.

[60] H. Mirzaee, L. Ji, J. Ryan, and R. Kirby. Smoothness-increasing accuracy-conserving (SIAC) post- processing for discontinuous Galerkin solutions over structured triangular meshes. *SIAM J. Numer. Anal.*, 49(5):1899–1920, 2011.

[61] P. Moujaes and D. Kuzmin. Monolithic convex limiting and implicit pseudo-time stepping for calculating steady-state solutions of the euler equations. *Journal of Computational Physics*, 523:113687, 2025.

[62] I. Navon. Finite-element simulation of the shallow-water equations model on a limited-area domain. *Appl. Math. Modelling*, 3, 1979.

[63] S. Noelle, Y. Xing, and C.-W. Shu. High-order well-balanced finite volume weno schemes for shallow water equation with moving water. *J. Comput. Phys.*, 226(1):29–58, 2007.

[64] H. T. Ozkan-Haller and J.T.Kirby. A fourier-chebyshev collocation method for the shallow water equations including shoreline. *Applied Ocean Research*, 19:21–34, 1997.

[65] P.-O.Persson and J.Peraire. Sub-cell shock capturing for discontinuous galerkin methods. *AIAA Aerospace Sciences Meeting and Exhibit*, 112, 2006.

[66] K. Panourgiasa and J. Ekaterinaris. A nonlinear filter for high order discontinuous Galerkin discretizations with discontinuity resolution within the cell. *J. Comput. Phys.*, 326:234–257, 2016.

[67] J. Patera and V. Nassehi. A new two-dimensional finite element model for the shallow water equations using a lagrangian framework constructed along fluid particle trajectories. *Int. J. Numer. Meth. Fluids*, 39:4159–4182, 1996.

[68] J. Qiu and C.-W. Shu. A comparison of troubled-cell indicators for Runge-Kutta discontinuous Galerkin methods using weighted essentially nonoscillatory limiters. *SIAM J. Sci. Comput.*, 27:995–1013, 2005.

[69] J. Qiu and C.-W. Shu. Runge Kutta discontinuous Galerkin method using WENO limiters. *SIAM J. Sci. Comput.*, 26:907–929, 2005.

[70] W. Reed and T. Hill. Triangular mesh methods for the neutron transport equation. *Los Alamos Scientific Laboratory Report*, LA-UR-73-479, 1973.

[71] B. Rogers, A. Borthwick, and P. Taylor. Mathematical balancing of flux gradient and source terms prior to using Roe's approximate riemann solver. *J. Comput. Phys.*, 192:422–451, 2003.

[72] A. Rueda-Ramirez, B. Bolm, D. Kuzmin, and G. Gassner. Monolithic convex limiting for legendre-gauss-lobatto discontinuous galerkin spectral-element methods. *Commun. Appl. Math. Comput.*, 2024.

[73] A. M. Rueda-Ramirez, W. Pazner, and G. J. Gassner. Subcell limiting strategies for discontinuous galerkin spectral element methods. *Computers and Fluids*, 247:105627, 2022.

[74] M. Sonntag and C. Munz. Shock capturing for discontinuous Galerkin methods using finite volume subcells. In *Finite Volumes for Complex Applications VII-Elliptic, Parabolic and Hyperbolic Problems*, pages 945–953, 2014.

[75] J. Tanner and E. Tadmor. Adaptive mollifiers - high resolution recover of piecewise smooth data from its spectral information. *Found. Comput. Math.*, 2:155–189, 2002.

[76] E. Toro. *Shock-capturing methods for free-surface shallow flows*. Chichester: John Wiley and Sons, 2001.

[77] T. Utnes. A finite element solution of the shallow-water wave equations. *Appl. Math. Modelling*, 14:20–29, 1990.

[78] J. Van der Vegt and H. Van der Ven. Space-time discontinuous Galerkin finite element method with dynamic grid motion for inviscid compressible flows. *J. Comput. Phys.*, 182:546–585, 2002.

[79] H. Vandeven. Family of spectral filters for discontinuous problems. *J. Sci. Comput.*, 8:159–192, 1991.

[80] F. Vilar. A posteriori correction of high-order discontinuous galerkin scheme through subcell finite volume formulation and flux reconstruction. *J. Comput. Phys.*, 387:245–279, 2019.

[81] F. Vilar. Local subcell monolithic DG/FV convex property preserving scheme on unstructured grids and entropy consideration. *J. Comput. Phys.*, 521(1), 2025.

[82] F. Vilar and R. Abgrall. A posteriori local subcell correction of high-order discontinuous galerkin scheme for conservation laws on two-dimensional unstructured grids. *SIAM Journal on Scientific Computing*, 46(2):A851–A883, 2024.

[83] F. Vilar, P. Maire, and R. Abgrall. Cell-centered discontinuous Galerkin discretizations for two-dimensional scalar conservation laws on unstructured grids and for one-dimensional Lagrangian hydrodynamics. *Comput. Fluids*, 46:498–504, 2011.

[84] S. Vukovic. Eno and weno schemes with the exact conservation property for one-dimensional shallow water equations. *J. Comput. Phys.*, 179(2):593–621, 2002.

[85] X. Wu, N. Trask, and J. Chan. Entropy stable discontinuous galerkin methods for the shallow water equations with subcell positivity preservation. *Numerical Methods for Partial Differential Equations*, 40(6):e23129, 2024.

[86] M. Zefzouf and F. Marche. A new symmetric interior penalty discontinuous galerkin formulation for the serre-green-naghdi equations. *Numer. Methods Partial Differential Eq.*, 39(2):1478–1503, 2023.

[87] J. Zhu, J. Qiu, C.-W. Shu, and M. Dumbser. Runge–Kutta discontinuous Galerkin method using WENO limiters II: Unstructured meshes. *J. Comput. Phys.*, 227:4330–4353, 2008.

[88] J. Zhu, X. Zhong, C.-W. Shu, and J. Qiu. Runge Kutta discontinuous Galerkin method using a new type of WENO type limiters on unstructured meshes. *J. Comp. Phys.*, 248:200–220, 2013.